

NuSTAR spectral analysis of three Seyfert galaxies: NGC 3227, NGC 5548 and MR 2251–178

Indrani Pal,¹ C. S. Stalin,¹ L. Mallick^{3,1} and Priyanka Rani²

¹ Indian Institute of Astrophysics, Bangalore, India
e-mail: indrani.pal@iiap.res.in

² Inter University Centre for Astronomy and Astrophysics, Pune, India

³ Cahill Center for Astronomy and Astrophysics, California Institute of Technology, Pasadena, CA 91125, USA

Received October 15, 2021; accepted February 28, 2022

ABSTRACT

Context. The observed nuclear X-ray emission in the radio-quiet category of active galactic nuclei (AGN) is believed to be from a compact region, the corona situated in the vicinity of the central supermassive black holes (SMBH). The shape of the X-ray continuum, among other factors, depends on the temperature of the corona (kT_e). The launch of the *Nuclear Spectroscopic Telescope Array (NuSTAR)* has led to the determination of the high energy cut-off (E_{cut} ; and thereby kT_e) in many AGN. In a handful of sources, multiple observations with *NuSTAR* have also revealed changes in E_{cut} .

Aims. In this work we aimed to investigate the variation in kT_e in three AGN, namely NGC 3227, NGC 5548 and MR 2251–178 using more than one epoch of data on a source from *NuSTAR*.

Methods. We carried out spectral analysis of multiple epochs of data acquired using *NuSTAR* on the three sources including a few new observations not published so far. By fitting Comptonization model to the data we determined the temperature of the corona and also investigated changes in kT_e if any in these sources.

Results. In NGC 3227, we found evidence for variation in kT_e . We found no correlation of kT_e , photon index (Γ), reflection fraction (R) and optical depth (τ) with flux, while, τ is found to anti-correlate with kT_e . These could be due to more than one physical process at work in the source that causes the change in kT_e . Conclusive evidence for the variation in kT_e is not found in MR 2251–178 and NGC 5548.

Key words. Galaxies: active – Galaxies: Seyfert – X-rays: galaxies

1. Introduction

Active galactic nuclei (AGN) are amongst the most luminous objects ($L = 10^{42} - 10^{46}$ erg s^{-1} ; Fabian 1999) in the Universe that emit radiation over a wide range of wavelengths. They are believed to be powered by accretion of matter onto SMBH ($10^5 - 10^9 M_{\odot}$) situated at the center of galaxies (Rees 1984; Dewangan et al. 2008). The SMBH is generally supposed to be surrounded by an optically thick and geometrically thin accretion disk (Shakura & Sunyaev 1973). The observed X-ray emission from the nuclear region of the radio-quiet category of AGN is believed to be produced by inverse Compton process, caused by the interaction of the seed ultra-violet (UV) photons from the accretion disk with the thermal electrons in a hot ($\sim 10^{8-9}$ K) region called the corona that is situated close to the accretion disk (Haardt & Maraschi 1991; Haardt et al. 1994). This X-ray continuum gets reprocessed in the accretion disk giving rise to the reflection hump at around 15–30 keV and also the broad FeK α line at 6.4 keV (George & Fabian 1991; Matt et al. 1993). Soft excess between 0.1 – 2 keV is ubiquitously observed in Type I AGN (Magdziarz et al. 1998; Fabian et al. 2002; Crummy et al. 2006; Bianchi et al. 2009; Gliozzi & Williams 2020), although the physical origin of this component remains

highly debated (García et al. 2019; Xu et al. 2021), different analyses showed that a two temperature Comptonization process agrees well with such a component either from an observational (e.g. Jin et al. 2012; Porquet et al. 2018; Petrucci et al. 2018; Middei et al. 2020; Matzeu et al. 2020) or theoretical (e.g. Rózańska et al. 2015; Petrucci et al. 2020; Ballantyne 2020; Ballantyne & Xiang 2020) point of view. Analysis of these spectral features (reflection, FeK α line, soft excess) will help in providing strong constraints on the nature of the X-ray emitting region. From X-ray reverberation studies (Fabian et al. 2009; Zoghbi et al. 2012) AGN corona is believed to be a compact region situated above the accretion disk typically within 3–10 R_G , where R_G is the gravitational radius and it is defined as, $R_G = GM_{BH}/c^2$, here M_{BH} is the SMBH mass and G is the gravitational constant. However, there are strong debates concerning the geometry of the corona. The lamp post is one such possibility but other models also exist (e.g. Haardt et al. 1994; Done et al. 2012; Petrucci et al. 2013). Also, rapid X-ray flux variability studies (McHardy et al. 2005), the observed small time scales of X-ray eclipses (Risaliti et al. 2005, 2011) and microlensing studies (Chartas et al. 2009) point to the small size of the X-ray corona of 5–10 R_G .

The observed shape of the X-ray continuum can be described by a power law with an exponential cut-off (E_{cut}), and the spectral shape depends on the optical depth (τ), temperature of the coronal plasma (kT_e), seed photon temperature and the viewing angle. From a study of the Seyfert galaxy NGC 5548, Petrucci et al. (2000) showed the existence of an approximate relation between E_{cut} and kT_e as $E_{\text{cut}} = 2\text{--}3 kT_e$. On analysis of a sample of Seyfert galaxies, according to Petrucci et al. (2001), for an optically thin corona with $\tau < 1$; $E_{\text{cut}} \approx 2 kT_e$, while for an optically thick corona with $\tau > 1$, $E_{\text{cut}} \approx 3 kT_e$. However, by fitting Comptonized spectra simulated using a range of τ and kT_e with a power law with an exponential cut-off model, Middei et al. (2019), showed that the commonly adopted relation of $E_{\text{cut}} = 2\text{--}3 kT_e$ is not valid for all values of τ and kT_e , instead valid for only low values of τ and kT_e .

Observations from high energy X-ray missions such as *CGRO* (Zdziarski et al. 2000; Johnson et al. 1997), *Bep-poSAX* (Nicastrò et al. 2000; Dadina 2007), *INTEGRAL* (Malizia et al. 2014; Lubiński et al. 2010, 2016; Ricci et al. 2011), *Swift*-BAT (Vasudevan et al. 2013b; Ricci et al. 2017); and *Suzaku* (Tazaki et al. 2011) showed that the corona in Seyfert galaxies has a wide range of temperature with E_{cut} ranging from 50 – 500 keV. However, observations from those missions are limited to bright and nearby sources. Thus, it is very clear that many efforts were put to measure E_{cut} in the X-ray spectra of several AGN. However, a major transformation in the studies of the Comptonization spectrum of AGN to determine E_{cut} from an epoch of observation happened after the launch of the *Nuclear Spectroscopic Telescope Array* (*NuSTAR*; Harrison et al. 2013) in the year 2012, owing to its broad spectral coverage of 3–79 keV and its high sensitivity beyond 10 keV. Since the launch of *NuSTAR*, E_{cut} values were obtained for many AGN (Fabian et al. 2017; Tortosa et al. 2018; Rani & Stalin 2018b,a; Rani et al. 2019; Lanzuisi et al. 2019; Baloković et al. 2020; Reeves et al. 2021; Kang et al. 2021). Importantly, in addition to the determination of E_{cut} values (and thereby constraining kT_e), in less than half-a-dozen sources there are also reports of variation in the E_{cut} values pointing to variations in kT_e .

For example in seven sources, namely MCG-5-23-16 (Zoghbi et al. 2017), 3C 382 (Ballantyne et al. 2014), NGC 4593 (Ursini et al. 2016), NGC 5548 (Ursini et al. 2015), Mrk 335 (Keek & Ballantyne 2016), NGC 3227 and SWIFT J2127.4+5654 (Kang et al. 2021) variations in the E_{cut} values are available in the literature. Recently, from a reanalysis of the *NuSTAR* spectra of five sources using a model independent approach, Zhang et al. (2018) confirmed the E_{cut} variation in three of the five sources namely 3C 382, NGC 5548 and Mrk 335. Most of these inferences were based on variations in E_{cut} obtained from phenomenological model fits to the data. However, to know changes in kT_e it is imperative to fit physical models to the data, because, it is known recently, that the relation $E_{\text{cut}} = 2\text{--}3 kT_e$ does not always hold true (Middei et al. 2019). Therefore it is imperative to fit physical model fits to the observed spectra to get kT_e . Though E_{cut} is known to vary, we do not yet know the causes for its variation. Despite that, it is important to increase the number of sources that show variation in the temperature of the corona. This is now achievable owing to the multiple-epochs of observation available on a

large number of AGN in the *NuSTAR* archives¹. The primary motivation here is, therefore to increase the number of AGN that show variation in kT_e . We are in the process of a careful and systematic investigation of kT_e variation in a large number of AGN. Here, we present the results from the multiple-epoch spectral analysis of three AGN, namely NGC 3227, NGC 5548 and MR 2251–178. This also includes few new observations not published so far.

NGC 3227, at a redshift of $z = 0.004$ and powered by a black hole of mass $4.79 \times 10^6 M_{\odot}$ (Bentz & Katz 2015), has been extensively studied in the X-ray band. Signatures of warm absorbers are evident in this source from observations with *ASCA* (Netzer et al. 1994; George et al. 1998), *ROSAT* (Komossa & Fink 1997) and *XMM-Newton* (Markowitz et al. 2009). In the *XMM-Newton* observations, FeK α line was evident (Markowitz et al. 2009). It has also been recently studied by Lobban et al. (2020) for flux variations combining *XMM-Newton* and *NuSTAR* observations. It has complex absorption features, which are also variable (Turner et al. 2018). Recently Mehdipour et al. (2021) has reported the broad band spectral modeling of the source using multi-wavelength data from *XMM-Newton*, *NuSTAR* and *Hubble Space Telescope* (*HST*). NGC 5548 is a galaxy located at $z = 0.017$ with a black hole of mass $5.0 \times 10^7 M_{\odot}$ (Bentz & Katz 2015). It has been extensively studied in the X-ray band using data from various satellites and has also been found to be strongly absorbed in soft X-rays (Cappi et al. 2016; Ursini et al. 2015; Mehdipour et al. 2015; Kaastra et al. 2014). MR 2251–178, with a black hole mass of $2.0 \times 10^8 M_{\odot}$ (Wang et al. 2009), first discovered by its strong X-ray emission (Ricker et al. 1978) was found to be a low redshift AGN at $z = 0.06$ (Bergeron et al. 1983). From VLA observations, Macchetto et al. (1990) found the source to show weak radio emission with elongated morphology resembling a FRI source. Details of the observations and reduction of the data are presented in Section 2, analysis is presented in Section 3, results and discussion are presented in Section 4 followed by the summary in the final section.

2. Observations and Data Reduction

2.1. Data reduction

We reduced *NuSTAR* data in the 3–79 keV band using the standard *NuSTAR* data reduction software NuSTARDAS² distributed by HEASARC within HEASoft v6.29. Considering the passage of the satellite through the South Atlantic Anomaly (SAA) we selected, SAACALC “2”, SAAMODE “optimized” and also excluded the tentacle region. The calibrated, cleaned, and screened event files were generated by running the *nupipeline* task using the CALDB release 20210701. To extract the source counts we chose a circular region of radius 60 arcsec centered on the source. Similarly, to extract the background counts, we selected a circular region of the same radius away from the source on the same chip to avoid contamination from source photons. We then used the *nuproducts* task to generate energy spectra, response matrix files (RMFs) and auxiliary response files (ARFs), for both the hard X-ray detectors housed

¹ <https://heasarc.gsfc.nasa.gov/cgi-bin/W3Browse/w3browse.pl>

² <https://heasarc.gsfc.nasa.gov/docs/nustar/analysis/nustar-swguide.pdf>

Table 1. Details of the sources analyzed in this work. The columns are (1) name of the source, (2) right ascension (h:m:s), (3) declination (d:m:s), (4) redshift, (5) galactic hydrogen column density N_{H} in units of 10^{22} atoms cm^{-2} obtained from Willingale et al. (2013), (6) type of the source, (7) observation ID, (8) epoch, (9) date of observation, and (10) exposure time in sec. The information such as the right ascension, declination and z are from Véron-Cetty & Véron (2010). The OBSIDs that are analysed for the first time are shown in bold.

Name	α_{2000}	δ_{2000}	z	N_{H}	Type	OBSID	Epoch	Date	Exposure
NGC 3227	10:23:30.60	+19:51:56	0.004	0.021	Sy1.5	60202002002	A	09-11-2016	49800
						60202002004	B	25-11-2016	42457
						60202002006	C	29-11-2016	39685
						60202002008	D	01-12-2016	41812
						60202002010	E	05-12-2016	40887
						60202002012	F	09-12-2016	39277
						60202002014	G	21-01-2017	47602
						80502609002	H	15-11-2019	28782
						80502609004	I	05-12-2019	27690
						NGC 5548	14:17:59.53	+25:08:12	0.017
60002044003	B	12-07-2013	27272						
60002044005	C	23-07-2013	49521						
60002044006	D	10-09-2013	51460						
60002044008	E	20-12-2013	50102						
90701601002	F	26-01-2021	38719						
60102025002	A	18-05-2015	23112						
MR 2251–178	22:54:05.90	−17:34:55	0.064	0.027	Sy1.5	60102025004	B	17-06-2015	23185
						60102025006	C	10-11-2015	20588
						60102025008	D	11-12-2015	21707
						90601637002	E	16-12-2020	23620

inside the corresponding focal plane modules FPMA and FPMB. For spectral analysis, using XSPEC version 12.12.0 (Arnaud 1996), we fitted the background subtracted spectra from FPMA and FPMB simultaneously (without combining them) allowing the cross normalization factor to vary freely during spectral fits. The spectra were binned to have a S/N ratio greater than 5 in each spectral channel using the *NuSTAR*-specific Python script *snrgppha*³. To get an estimate of the model parameters that best describe the observed data, we used the chi-square (χ^2) statistics and for calculating the errors in the model parameters we used the $\chi^2 = 2.71$ criterion i.e. 90 per cent confidence range in XSPEC.

3. Analysis of the data

For few epochs of the sources studied in this work, we do have observations in the soft band from telescopes such as *XMM-Newton* for NGC 3227 and *XMM-Newton*, *Chandra* for NGC 5548 and *XMM-Newton* for MR 2251–178. However, for this work, we decided to use only *NuSTAR* data as (a) the good sensitivity of *NuSTAR* over the 3–79 keV energy band captures all the key reflection features of an AGN spectrum and as the main goal of this work is to model the high energy rollover of the Comptonized spectra we did not want the absorption in the soft band affecting our analysis in the determination of kT_e and (b) observations in the soft band are not available simultaneous to the *NuSTAR* observations for all the epochs and for all the sources. However we note here, the inclusion of soft X-ray data in the fitting might have an effect on the photon index (Γ) obtained from using the *NuSTAR* data alone. However, a simplest approach to constrain kT_e (which is the aim of this work) is the use of only *NuSTAR* data, but for better constraining

the other physical characteristics of the sources broad band spectral analysis including data from UV to hard X-ray band is more appropriate. While analyzing only *NuSTAR* data, we ignored the 3–4 keV band to limit the effect of absorption if any and also did not consider data in the energy range beyond 60 keV due to lack of source photons. Thus, we carried out spectral fits to the *NuSTAR* data in the 4–60 keV energy band for all the OBSIDS except for epoch I of NGC 3227, epoch F of NGC 5548 and epoch E of MR 2251–178. Due to the unavailability of photons beyond 50 keV we restricted the spectral fit in the 4–50 keV energy band to the epoch I and epoch E spectra of NGC 3227 and MR 2251–178 respectively. Similarly, for the epoch F spectrum of NGC 5548, we used the FPMA/FPMB data in the 4–55 keV range. (see Fig 1).

3.1. Phenomenological spectral fits

For our spectral fits, to model the line of sight galactic absorption, the value of the neutral hydrogen column density (N_{H}) for all the sources were frozen to the values obtained from Willingale et al. (2013). These N_{H} values are given in Table 1. Similarly, the redshifts of the sources were frozen to their corresponding values given in Table 1. Also, we used the solar abundances from Wilms et al. (2000) and the photoelectric cross sections from Verner et al. (1996). For models that require inclination angle (i), we used $i = 50^\circ$ for NGC 3227 (Schmitt et al. 1997, Alonso-Herrero et al. 2019, Middleton et al. 2016), $i = 30^\circ$ for NGC 5548 (Ursini et al. 2015) and $i = 60^\circ$ (i.e., the default value) for MR 2251–178.

3.1.1. Absorbed power law

Firstly, to understand the continuum emission in our sample of sources we fitted the observed X-ray spectra with the

³ <https://sites.astro.caltech.edu/~mislavb/>

Table 2. Results of the fit to the spectra of NGC 3227. The models are Model I: $const * TBabs * zTBabs(zpo + zgauss)$, Model II: $const * TBabs * zTBabs(pexrav + zgauss)$, Model III: $const * TBabs * zTBabs(xillver)$ and Model IV: $const * TBabs * zTBabs(xillverCP)$. The $zTBabs$ component is added with all the models to fit the epoch G, H and I spectra. The fluxes are in units of 10^{-10} erg $cm^{-2} s^{-1}$ in the 4–60 keV band except in epoch I where the flux was calculated in 4–50 keV band. Energy (E) of the FeK α line, equivalent width (EW) of the line, E_{cut} and kT_e are expressed in units of keV, model normalization is in units of 10^{-4} photons $keV^{-1} cm^{-2} s^{-1}$ and $N_H(zTBabs)$ is the host galaxy hydrogen column density in units of 10^{22} atoms cm^{-2} . $C_{FPMA/FPMB}$ is the cross-calibration constant. The width of the FeK α line was fixed to 0.1 keV during the fitting.

Parameter	epoch A	epoch B	epoch C	epoch D	epoch E	epoch F	epoch G	epoch H	epoch I
Model I : $const * TBabs * zTBabs(zpo + zgauss)$									
Γ	1.56 ^{+0.01} _{-0.01}	1.55 ^{+0.01} _{-0.01}	1.61 ^{+0.01} _{-0.01}	1.63 ^{+0.01} _{-0.01}	1.66 ^{+0.01} _{-0.01}	1.63 ^{+0.01} _{-0.01}	1.61 ^{+0.02} _{-0.02}	1.64 ^{+0.04} _{-0.04}	1.48 ^{+0.07} _{-0.07}
$N_H(zTBabs)$	-	-	-	-	-	-	2.91 ^{+1.04} _{-1.03}	4.66 ^{+1.83} _{-1.80}	4.57 ^{+3.73} _{-3.62}
E	6.35 ^{+0.03} _{-0.03}	6.38 ^{+0.03} _{-0.04}	6.33 ^{+0.04} _{-0.04}	6.32 ^{+0.04} _{-0.03}	6.30 ^{+0.05} _{-0.05}	6.34 ^{+0.05} _{-0.05}	6.23 ^{+0.04} _{-0.04}	6.28 ^{+0.07} _{-0.07}	6.38 ^{+0.05} _{-0.05}
EW	149 ⁺²³ ₋₃₂	188 ⁺³² ₋₄₂	142 ⁺³⁰ ₋₃₅	129 ⁺²² ₋₂₄	86 ⁺²⁶ ₋₃₀	115 ⁺²⁶ ₋₃₈	115 ⁺²³ ₋₂₃	123 ⁺⁴⁴ ₋₄₀	269 ⁺⁸⁶ ₋₈₁
norm	71 ⁺² ₋₂	58 ⁺² ₋₂	73 ⁺² ₋₂	90 ⁺³ ₋₃	101 ⁺³ ₋₃	92 ⁺³ ₋₃	122 ⁺⁷ ₋₆	76 ⁺⁸ ₋₇	17 ⁺⁴ ₋₃
χ^2/dof	930/826	752/706	834/704	909/777	815/790	684/717	1081/935	600/595	257/247
$C_{FPMA/FPMB}$	1.04 ^{+0.01} _{-0.01}	1.02 ^{+0.01} _{-0.01}	1.01 ^{+0.01} _{-0.01}	1.01 ^{+0.01} _{-0.01}	1.02 ^{+0.01} _{-0.01}	1.00 ^{+0.01} _{-0.01}	0.99 ^{+0.01} _{-0.01}	1.04 ^{+0.01} _{-0.01}	1.06 ^{+0.03} _{-0.03}
Model II : $const * TBabs * zTBabs(pexrav + zgauss)$									
Γ	1.68 ^{+0.05} _{-0.05}	1.64 ^{+0.06} _{-0.05}	1.77 ^{+0.05} _{-0.05}	1.83 ^{+0.04} _{-0.04}	1.88 ^{+0.05} _{-0.05}	1.82 ^{+0.05} _{-0.05}	1.92 ^{+0.01} _{-0.07}	1.85 ^{+0.08} _{-0.08}	1.70 ^{+0.04} _{-0.11}
$N_H(zTBabs)$	-	-	-	-	-	-	6.43 ^{+0.92} _{-1.42}	7.71 ^{+1.93} _{-1.95}	8.52 ^{+4.30} _{-5.18}
E_{cut}	212 ⁺¹⁴⁰ ₋₆₃	163 ⁺¹¹⁸ ₋₅₀	>254	>1147	>411	>406	>571	>775	>126
R	0.52 ^{+0.15} _{-0.13}	0.48 ^{+0.18} _{-0.15}	0.53 ^{+0.18} _{-0.15}	0.55 ^{+0.16} _{-0.14}	0.73 ^{+0.19} _{-0.17}	0.55 ^{+0.18} _{-0.16}	0.83 ^{+0.16} _{-0.15}	0.45 ^{+0.20} _{-0.18}	0.38 ^{+0.49} _{-0.34}
E	6.35 ^{+0.03} _{-0.03}	6.38 ^{+0.04} _{-0.04}	6.33 ^{+0.04} _{-0.04}	6.32 ^{+0.04} _{-0.04}	6.31 ^{+0.06} _{-0.06}	6.34 ^{+0.05} _{-0.05}	6.23 ^{+0.04} _{-0.04}	6.28 ^{+0.07} _{-0.07}	6.38 ^{+0.06} _{-0.06}
EW	137 ⁺³² ₋₂₀	177 ⁺³⁷ ₋₄₂	129 ⁺²⁶ ₋₃₃	116 ⁺²⁵ ₋₂₃	74 ⁺²⁶ ₋₂₁	102 ⁺³² ₋₂₂	85 ⁺²³ ₋₁₉	102 ⁺³⁴ ₋₃₁	231 ⁺⁸² ₋₇₄
norm	84 ⁺⁶ ₋₆	66 ⁺⁶ ₋₅	91 ⁺⁸ ₋₇	119 ⁺⁸ ₋₇	139 ⁺¹⁰ ₋₁₀	120 ⁺⁹ ₋₉	207 ⁺¹⁹ ₋₂₅	112 ⁺¹⁸ ₋₁₆	25 ⁺⁹ ₋₉
χ^2/dof	856/824	711/704	784/702	831/775	714/788	625/715	920/933	577/593	253/245
$C_{FPMA/FPMB}$	1.04 ^{+0.01} _{-0.01}	1.02 ^{+0.01} _{-0.01}	1.01 ^{+0.01} _{-0.01}	1.01 ^{+0.01} _{-0.01}	1.02 ^{+0.01} _{-0.01}	1.00 ^{+0.01} _{-0.01}	0.99 ^{+0.01} _{-0.01}	1.04 ^{+0.01} _{-0.01}	1.06 ^{+0.03} _{-0.03}
Model III : $const * TBabs * zTBabs(xillver)$									
Γ	1.69 ^{+0.01} _{-0.01}	1.69 ^{+0.01} _{-0.01}	1.77 ^{+0.02} _{-0.01}	1.83 ^{+0.01} _{-0.01}	1.80 ^{+0.01} _{-0.01}	1.79 ^{+0.01} _{-0.01}	1.77 ^{+0.01} _{-0.01}	1.87 ^{+0.02} _{-0.02}	1.91 ^{+0.03} _{-0.03}
$N_H(zTBabs)$	-	-	-	-	-	-	4.73 ^{+0.57} _{-0.56}	8.58 ^{+0.98} _{-1.08}	12.12 ^{+1.86} _{-1.82}
E_{cut}	127 ⁺¹⁴ ₋₁₂	92 ⁺¹⁰ ₋₈	204 ⁺⁴⁶ ₋₃₄	>439	378 ⁺¹⁵² ₋₉₁	326 ⁺¹²³ ₋₇₈	248 ⁺⁶⁷ ₋₃₄	>510	>198
R	0.86 ^{+0.12} _{-0.12}	1.09 ^{+0.17} _{-0.16}	0.85 ^{+0.14} _{-0.13}	0.76 ^{+0.14} _{-0.12}	0.61 ^{+0.12} _{-0.09}	0.71 ^{+0.14} _{-0.11}	0.68 ^{+0.08} _{-0.08}	0.64 ^{+0.16} _{-0.14}	1.36 ^{+0.47} _{-0.40}
norm	1.98 ^{+0.02} _{-0.03}	1.46 ^{+0.02} _{-0.05}	2.01 ^{+0.03} _{-0.03}	2.98 ^{+0.04} _{-0.04}	2.97 ^{+0.03} _{-0.03}	2.75 ^{+0.04} _{-0.04}	3.73 ^{+0.04} _{-0.04}	2.72 ^{+0.03} _{-0.04}	0.68 ^{+0.03} _{-0.03}
χ^2/dof	868/826	728/706	785/704	837/777	735/790	627/717	976/935	579/595	260/247
$C_{FPMA/FPMB}$	1.04 ^{+0.01} _{-0.01}	1.02 ^{+0.01} _{-0.01}	1.01 ^{+0.01} _{-0.01}	1.01 ^{+0.01} _{-0.01}	1.02 ^{+0.01} _{-0.01}	1.00 ^{+0.01} _{-0.01}	0.99 ^{+0.01} _{-0.01}	1.04 ^{+0.01} _{-0.01}	1.06 ^{+0.03} _{-0.03}
Model IV : $const * TBabs * zTBabs(xillverCP)$									
Γ	1.78 ^{+0.01} _{-0.01}	1.80 ^{+0.01} _{-0.01}	1.83 ^{+0.01} _{-0.01}	1.84 ^{+0.01} _{-0.01}	1.83 ^{+0.01} _{-0.01}	1.83 ^{+0.01} _{-0.01}	1.82 ^{+0.01} _{-0.01}	1.87 ^{+0.02} _{-0.02}	1.91 ^{+0.04} _{-0.03}
$N_H(zTBabs)$	-	-	-	-	-	-	4.97 ^{+0.59} _{-0.55}	8.17 ^{+0.99} _{-0.82}	12.21 ^{+1.73} _{-1.65}
kT_e	33 ⁺⁹ ₋₇	28 ⁺⁹ ₋₆	56 ⁺¹³¹ ₋₁₈	>80	>45	>47	50 ⁺³⁹ ₋₁₀	>85	>36
R	0.79 ^{+0.11} _{-0.11}	0.96 ^{+0.18} _{-0.10}	0.83 ^{+0.15} _{-0.15}	0.78 ^{+0.13} _{-0.12}	0.62 ^{+0.11} _{-0.11}	0.71 ^{+0.14} _{-0.13}	0.67 ^{+0.09} _{-0.10}	0.65 ^{+0.16} _{-0.15}	1.28 ^{+0.60} _{-0.30}
norm	1.94 ^{+0.02} _{-0.02}	1.52 ^{+0.02} _{-0.02}	1.89 ^{+0.03} _{-0.03}	2.56 ^{+0.02} _{-0.03}	2.55 ^{+0.03} _{-0.05}	2.50 ^{+0.04} _{-0.04}	3.32 ^{+0.03} _{-0.07}	2.24 ^{+0.07} _{-0.05}	0.66 ^{+0.02} _{-0.02}
χ^2/dof	881/826	746/706	790/704	838/777	733/790	629/717	970/935	581/595	261/247
$C_{FPMA/FPMB}$	1.04 ^{+0.01} _{-0.01}	1.02 ^{+0.01} _{-0.01}	1.01 ^{+0.01} _{-0.01}	1.01 ^{+0.01} _{-0.01}	1.02 ^{+0.01} _{-0.01}	1.00 ^{+0.01} _{-0.01}	0.99 ^{+0.01} _{-0.01}	1.04 ^{+0.01} _{-0.01}	1.06 ^{+0.03} _{-0.03}
Flux	1.04 ^{+0.02} _{-0.01}	0.86 ^{+0.01} _{-0.01}	0.94 ^{+0.01} _{-0.02}	1.11 ^{+0.01} _{-0.01}	1.15 ^{+0.01} _{-0.02}	1.13 ^{+0.01} _{-0.01}	1.55 ^{+0.01} _{-0.01}	0.88 ^{+0.01} _{-0.01}	0.27 ^{+0.01} _{-0.01}

baseline phenomenological absorbed power law model and having the following form in XSPEC

$$const * TBabs(zpo) \quad (1)$$

The first component of this model is the constant used to calibrate the two focal plane modules of *NuSTAR*. The second component, *TBabs* (Wilms et al. 2000) was used to model the line of sight galactic absorption. The parameters that were kept free are Γ and the normalization (i.e. photons $keV^{-1} cm^{-2} s^{-1}$). We found evidence of intrinsic absorption present in the lower energy end for all the epochs in NGC 5548, epoch G, H and I in NGC 3227 and epoch E in MR 2251–178. We therefore included a $zTBabs$ component with the absorbed power law model to fit their spectra and the

model looks like

$$const * TBabs * zTBabs(zpo) \quad (2)$$

in XSPEC. For all epochs in NGC 5548, two epochs in NGC 3227 and one epoch of MR 2251–178 non-inclusion of $zTBabs$ returned a poor fit with χ^2/dof larger than 1.2. Inclusion of $zTBabs$ with $N_H(zTBabs)$ kept free improved the fit with χ^2/dof close to unity.

From the residual spectra obtained from the simple absorbed power law model fit to the observations, we noticed the presence of the fluorescent FeK α line in NGC 3227, NGC 5548 and in epoch D spectra of MR 2251–178, but in the other observations of MR 2251–178, the residual spectra do not show conspicuous FeK α line. The spectral fits are shown in Fig. 1 for NGC 3227 and NGC

Table 3. Results of the model fits to the spectra of MR 2251–178. The models are Model I: $const*TBabs*zTBabs(zpo)$, Model II: $const*TBabs*zTBabs(pearav)$, Model III: $const*TBabs*zTBabs(xillver)$ and Model IV: $const*TBabs*zTBabs(xillverCP)$. The $zTBabs$ component is added with all the models to fit the epoch E spectra. In epoch D the width of the $FeK\alpha$ line was fixed to 0.1 keV. In the case where no line was detected, the upper limit on the EW was calculated by fixing the line energy to 6.4 keV. The fluxes are in units of 10^{-10} erg cm^{-2} s^{-1} in the 4–60 keV band except in epoch E where the flux was calculated in 4–50 keV band. Columns and parameters have the same meaning as given in Table 2.

Parameter	epoch A	epoch B	epoch C	epoch D	epoch E
Model I : $const*TBabs*zTBabs(zpo+zgauss)$					
Γ	$1.75^{+0.02}_{-0.02}$	$1.79^{+0.01}_{-0.01}$	$1.79^{+0.02}_{-0.02}$	$1.79^{+0.02}_{-0.02}$	$1.83^{+0.05}_{-0.05}$
$N_H(zTBabs)$	-	-	-	-	$7.82^{+2.99}_{-2.93}$
E	-	-	-	$6.49^{+0.37}_{-0.27}$	-
EW	<35	<49	<34	<70	<46
norm	142^{+5}_{-5}	177^{+6}_{-6}	162^{+6}_{-6}	162^{+6}_{-6}	84^{+13}_{-11}
χ^2/dof	583/601	656/633	574/551	516/576	446/400
$C_{FPMA/FPMB}$	$1.02^{+0.02}_{-0.02}$	$1.00^{+0.01}_{-0.01}$	$1.03^{+0.02}_{-0.02}$	$1.02^{+0.02}_{-0.02}$	$1.05^{+0.02}_{-0.02}$
Model II : $const*TBabs*zTBabs(pearav+zgauss)$					
Γ	$1.65^{+0.05}_{-0.05}$	$1.72^{+0.05}_{-0.03}$	$1.76^{+0.07}_{-0.07}$	$1.79^{+0.06}_{-0.06}$	$1.82^{+0.11}_{-0.10}$
$N_H(zTBabs)$	-	-	-	-	$7.66^{+3.26}_{-3.02}$
E_{cut}	125^{+96}_{-39}	185^{+200}_{-69}	110^{+70}_{-32}	193^{+417}_{-80}	>175
R	<0.07	<0.11	$0.29^{+0.22}_{-0.18}$	$0.19^{+0.20}_{-0.17}$	<0.23
E	-	-	-	$6.48^{+0.67}_{-0.31}$	-
EW	<49	<43	<33	<63	<50
norm	111^{+8}_{-8}	144^{+11}_{-6}	139^{+15}_{-13}	144^{+15}_{-13}	75^{+19}_{-14}
χ^2/dof	569/599	647/631	552/549	509/574	446/398
$C_{FPMA/FPMB}$	$1.02^{+0.02}_{-0.02}$	$1.00^{+0.01}_{-0.01}$	$1.03^{+0.02}_{-0.02}$	$1.02^{+0.02}_{-0.02}$	$1.05^{+0.02}_{-0.02}$
Model III : $const*TBabs*zTBabs(xillver)$					
Γ	$1.65^{+0.02}_{-0.02}$	$1.72^{+0.02}_{-0.02}$	$1.70^{+0.02}_{-0.02}$	$1.77^{+0.02}_{-0.02}$	$1.82^{+0.02}_{-0.03}$
$N_H(zTBabs)$	-	-	-	-	$7.56^{+1.69}_{-1.38}$
E_{cut}	124^{+22}_{-18}	169^{+45}_{-30}	103^{+18}_{-14}	163^{+46}_{-30}	>366
R	<0.10	<0.16	$0.17^{+0.14}_{-0.13}$	$0.22^{+0.15}_{-0.13}$	<0.11
norm	$2.92^{+0.02}_{-0.04}$	$3.54^{+0.03}_{-0.05}$	$2.79^{+0.05}_{-0.05}$	$3.05^{+0.02}_{-0.02}$	$2.10^{+0.03}_{-0.52}$
χ^2/dof	569/599	647/631	556/549	510/576	447/398
$C_{FPMA/FPMB}$	$1.02^{+0.02}_{-0.02}$	$1.00^{+0.01}_{-0.01}$	$1.03^{+0.02}_{-0.02}$	$1.02^{+0.02}_{-0.02}$	$1.05^{+0.02}_{-0.02}$
Model IV : $const*TBabs*zTBabs(xillverCP)$					
Γ	$1.76^{+0.01}_{-0.01}$	$1.79^{+0.01}_{-0.01}$	$1.80^{+0.02}_{-0.01}$	$1.83^{+0.02}_{-0.01}$	$1.83^{+0.02}_{-0.02}$
$N_H(zTBabs)$	-	-	-	-	$7.54^{+1.42}_{-1.45}$
kT_e	25^{+26}_{-6}	35^{+149}_{-11}	21^{+8}_{-4}	35^{+67}_{-11}	>32
R	<0.06	<0.11	<0.25	$0.17^{+0.14}_{-0.13}$	<0.09
norm	$2.68^{+0.02}_{-0.03}$	$3.26^{+0.03}_{-0.05}$	$2.66^{+0.04}_{-0.04}$	$2.85^{+0.04}_{-0.04}$	$1.71^{+0.02}_{-0.04}$
χ^2/dof	576/599	650/631	555/549	511/576	447/398
$C_{FPMA/FPMB}$	$1.02^{+0.02}_{-0.02}$	$1.00^{+0.01}_{-0.01}$	$1.03^{+0.02}_{-0.02}$	$1.02^{+0.02}_{-0.02}$	$1.05^{+0.02}_{-0.02}$
Flux	$1.07^{+0.01}_{-0.01}$	$1.22^{+0.01}_{-0.01}$	$1.08^{+0.01}_{-0.01}$	$1.09^{+0.01}_{-0.01}$	$0.47^{+0.02}_{-0.01}$

5548 and MR 2251–178. Though this line is common in most of the X ray spectra of AGN (Mushotzky et al. 1993; Nandra et al. 2007; Della Ceca et al. 2010) there are exceptions (Bhayani & Nandra 2011). The apparent non-detection of $FeK\alpha$ line in the spectra of MR 2251–178 could be due to weaker reflection owing to larger viewing angle (Bhayani & Nandra 2011), low signal-to-noise ratio spectra, very high ionized accretion disk (Ross & Fabian 1993; Zycki & Czerny 1994) or a combination of all. However, the presence of a weak $FeK\alpha$ line in epoch D of MR 2251–178 could point to the physical characteristic of MR 2251–178 being different from the other two sources. A thorough analysis is needed to know the exact reasons for the absence/weakness of this line but this issue is beyond the scope of this work as we are in this work mainly interested in the changes in the temperature of the corona. To model the $FeK\alpha$ line seen in the residual spectra in NGC 3227, NGC

5548 and in one observation (epoch D) of MR 2251–178, we included a gaussian component and with this inclusion the model takes the form $const*TBabs(zpo + zgauss)$ and the quality of the fit improved.

After the inclusion of a gaussian component with the power law in the case of NGC 3227, in all nine epochs the χ^2 value reduced in the range between 60 and 242 for a reduction of 2 dof. In epochs C, D, G and I, non-inclusion of the gaussian component, resulted in a reduced χ^2 greater than 1.30. After the inclusion of the gaussian component the reduced χ^2 ranged between 1.04–1.16 in these epochs. For the other epochs, the χ^2/dof was > 1.1 before and it became ~ 1.0 after the line inclusion. For MR2251–178, gaussian component was used to fit the $FeK\alpha$ line only in epoch D. Inclusion of the line component lead to a change in χ^2 of 5 for a reduction of 2 dof. This negligible change in χ^2 over 2 dof did not improve the fit quality significantly

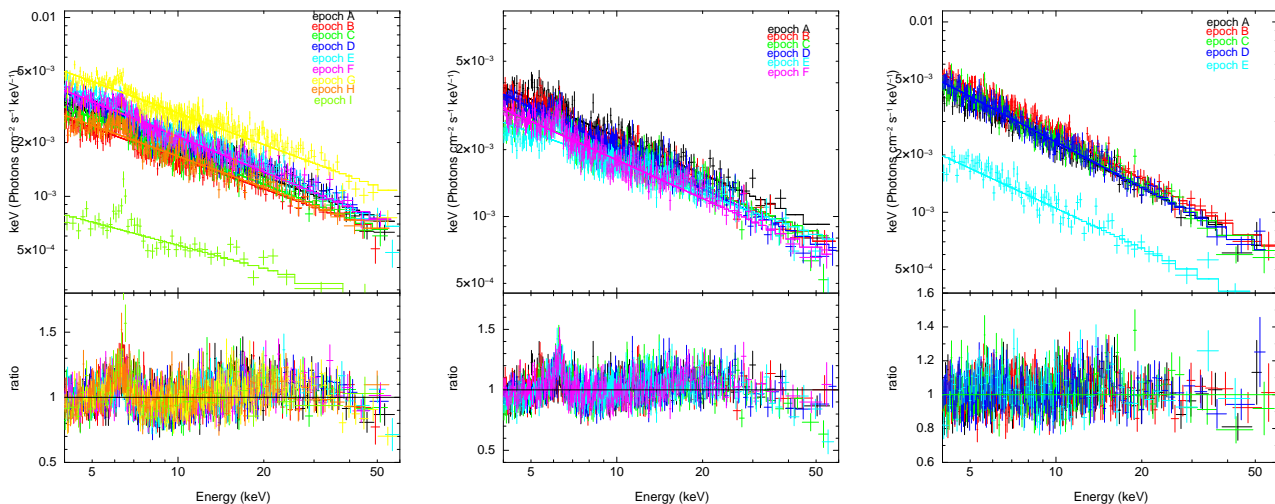


Fig. 1. The unfolded spectra of the nine observations for NGC 3227 (left), six observations for NGC 5548 (middle) and five observations for MR 2251–178 (right) fitted with a simple power-law. The bottom panels show the ratio of the observed spectra to the model. For clarity, we used only FPMA data. The spectra are rebinned for visualization purpose only.

in this case. For NGC 5548, on inclusion of gaussian line component in all the epochs, the value of the χ^2 reduced in the range 23 to 105 for a reduction of 2 dof. Just an absorbed power law fit to the data produced the reduced χ^2 greater than 1.2 for the epochs C, D, E and F. Adding the Gaussian with the power law lead to a reduced χ^2 of ~ 1.1 for epoch C and D and ~ 1.0 for epoch E and F. Similarly, for epochs A and B, the χ^2/dof changed from 1.10 to 1.06 and 1.02 to 0.97 respectively. The width of the FeK α line was frozen to the value of 0.1 keV during the fitting, letting it free to vary did not improve the fit significantly. The best fit parameters for the sources are given in Table 2, 3 and 4 for NGC 3227, MR 2251–178 and NGC 5548.

3.1.2. Pexrav

In the residuals of the simple power law fit to all the spectra of the sources (see Fig. 1) we found the signature of a high energy turn over and a reflection hump beyond 15 keV. To appropriately model both the high energy cut off and the reflection feature present in the spectra we replaced the *zpo* component in our earlier model with *pexrav* and the new model has the form

$$const * TBabs(pexrav). \quad (3)$$

While modelling the reflection component of NGC 5548, epoch G, H and I spectra of NGC 3227 and epoch E spectrum of MR 2251–178 an intrinsic absorption component, *zTBabs* was added with the above model. The intrinsic hydrogen column density, $N_H(zTBabs)$ was kept free during the fit.

This model implements both photoelectric absorption and Compton scattering, however, it does not include fluorescence. Therefore to model the FeK α line seen in the residual spectra in NGC 3227, NGC 5548 and epoch D in MR 2251–178, we included a gaussian component. So, the model takes the following form,

$$const * TBabs(pexrav + zgauss) \quad (4)$$

in XSPEC. The model *pexrav* improved the fitting compared to *zpo* as evident in the reduced χ^2 in Tables 2, 3 and

4. This model includes primary emission having a power law form with an exponential cut-off and a reflection component. The reflector is considered to be an optically thick medium in an infinite plane geometry and covering a larger fraction of the X-ray source. A parameter that comes as an output in the model fit is the reflection parameter *R*. This parameter gives a measure of the reflection component present in the observed spectra of the sources. For an isotropic source, this parameter is related to the solid angle (Ω) as $R \sim \Omega/2\pi$, and it is dependent on the angle of inclination (*i*) between the perpendicular to the accretion disk and the line of sight to the observer. The width of the FeK α line was fixed at 0.1 keV, treating the parameter free did not improve the fit. For all the sources, the parameters that were left free in the model fits are E_{cut} , Γ , *R* and normalization.

Using (*pexrav+zgauss*) in all the nine epochs of NGC 3227, the χ^2 reduced in the range between 4 and 161 for a reduction of 2 dof compared to the (*zpo+zgauss*) fit. In MR 2251–178, the reduction in χ^2 is in the range between 0 and 22 with a reduction of 2 in dof. For all the six epochs in NGC 5548, the (*pexrav+zgauss*) fit produced a reduction in the χ^2 values between 9–60 with a reduction of 2 dof compared to (*zpo+zgauss*). The best fit parameters are given in Tables 2, 3 and 4.

3.2. Physical model fits

3.2.1. xillver and xillverCP

Accretion disk reflection features in the form of narrow FeK α line was conspicuously present in the residuals of NGC 3227, NGC 5548 and epoch D spectra of MR 2251–178 and the line was modelled using a gaussian component in *pexrav* model fits. For MR 2251–178 we have seen signatures of reflection (though weak) in few epochs. This is evident from the best fit values of the reflection fraction obtained using *pexrav* (see Table 3) and in the residuals of the *zpo* model fits (see Fig. 4: top panel). We therefore modelled the spectra of the sources with the self consistent ionized reflection model *xillver*(García & Kallman 2010; García et al.

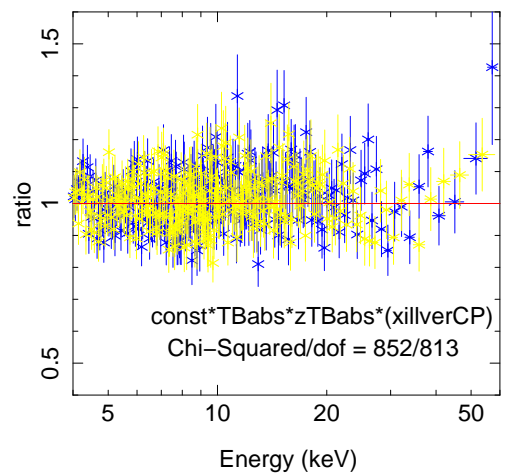
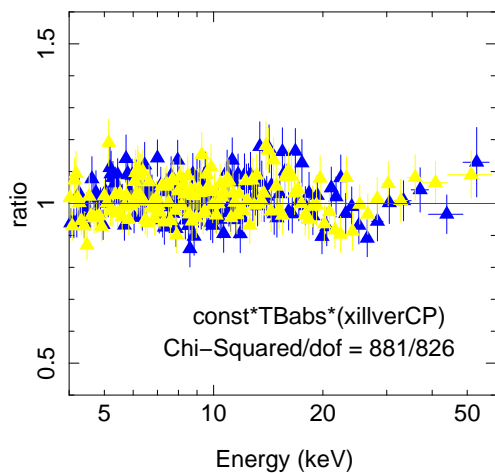
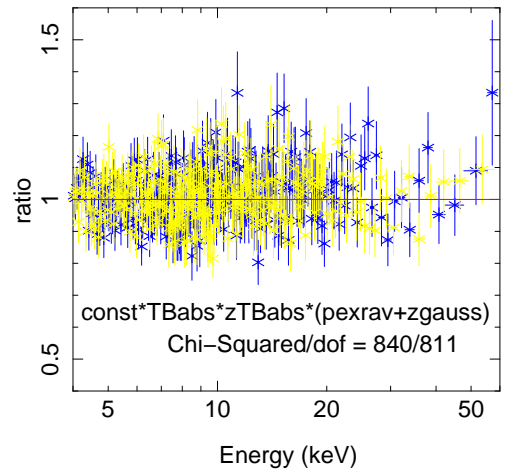
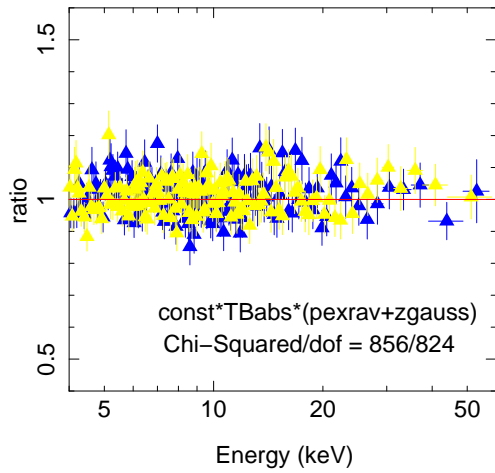
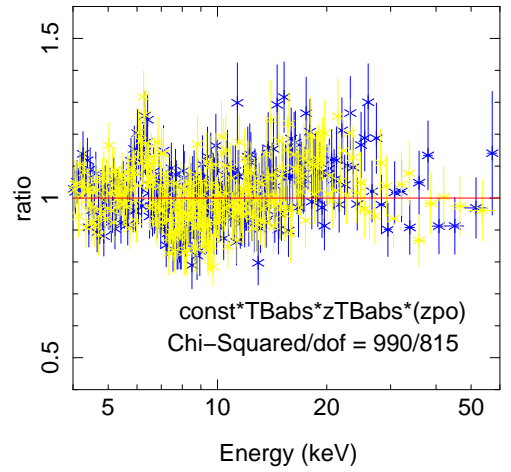
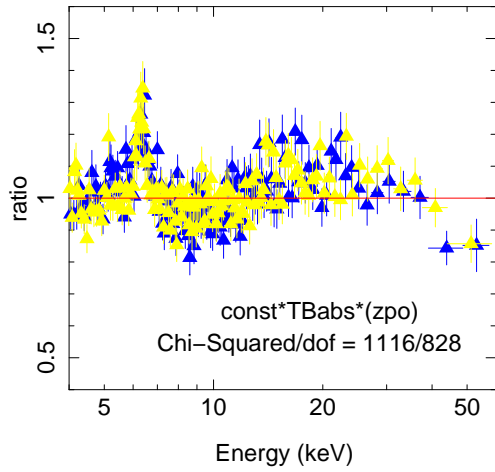


Fig. 2. Ratio of data to the model for the model fits $\text{const*TBabs}(zpo+zgauss)$, $\text{const*TBabs}(pexrav+zgauss)$ and $\text{const*TBabs}(xillverCP)$ to the FPMA (blue triangle) and FPMB (yellow triangle) spectra of OBID 60202002002 of NGC 3227. The spectra are rebinned for visualization purpose.

Fig. 3. Ratio plots for the model fits $\text{const*TBabs*zTBabs}(zpo+zgauss)$, $\text{const*TBabs*zTBabs}(pexrav+zgauss)$ and $\text{const*TBabs*zTBabs}(xillverCP)$ to the FPMA (blue star) and FPMB (yellow star) spectra of OBID 60002044006 of NGC 5548. The spectra are rebinned for visualization purpose only.

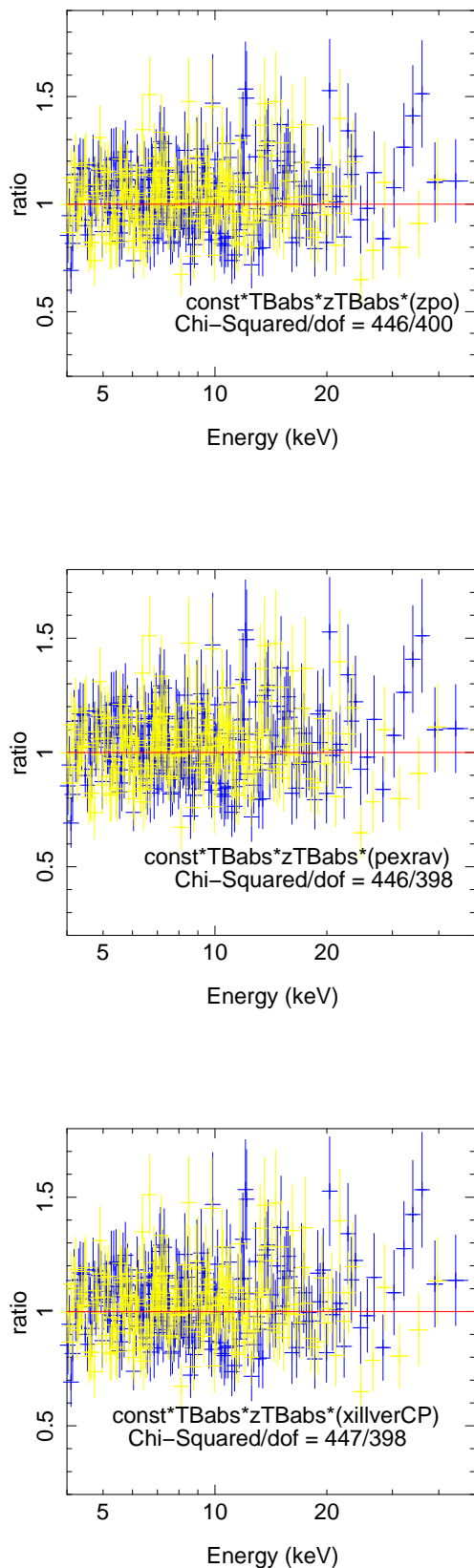


Fig. 4. Ratio of data to model for the model fits $const*TBabs*zTBabs*(zpo)$, $const*TBabs*zTBabs*(pexrav)$ and $const*TBabs*zTBabs*(xillverCP)$ to the FPMA (blue dot) and FPMB (yellow dot) spectra of OBID 90601637002 of MR 2251–178. We re-binned the spectra for visualization purpose only.

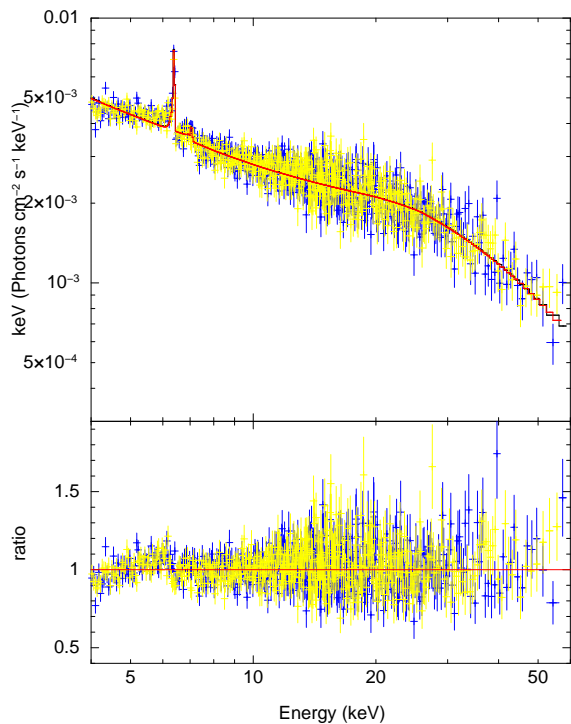


Fig. 5. The unfolded spectra with the ratio of data to model for the model fits $const*TBabs(xillverCP)$ to the FPMA (blue) and FPMB (yellow) spectra of OBID 60202002014 (epoch G) of NGC 3227.

2013). The emergent reflected spectrum from the surface of the X-ray illuminated accretion disk is calculated in the model by solving the equations of radiative transfer, energy balance and ionization equilibrium in a Compton thick plane parallel medium (García et al. 2013). The model fit to the spectra has the following form in XSPEC,

$$const * TBabs(xillver) \quad (5)$$

Here also, to account for the effect of intrinsic absorption, $zTBabs$ was used for all epochs of NGC 5548, three epochs (G, H and I) of NGC 3227 and epoch E of MR 2251–178. The intrinsic hydrogen column densities, $N_H(zTBabs)$ were kept as free parameters. In this model fit, the parameters describing the properties of the corona such as Γ , E_{cut} and R were made to vary, while the inclination angle was frozen to the value of 50° for NGC 3227, 30° for NGC 5548 and 60° for MR 2251–178. The other parameter that was kept free is the normalization. To account for a fair comparison between the E_{cut} values obtained from $pexrav$ and $xillver$ the reflector was assumed to be neutral i.e. $\log \zeta = 0 \text{ erg cm s}^{-1}$. Treating the ionization as a free parameter too, returned results consistent with the ones obtained using $\log \zeta = 0 \text{ erg cm s}^{-1}$. The value of Fe abundance was fixed to the solar value. The results of the model fits are given in Tables 2, 3 and 4. Fitting the spectra using $xillver$ yielded values of E_{cut} similar to that obtained using $pexrav$, although the errors in the E_{cut} measurements using $xillver$ are relatively smaller.

As we are interested in the determination of kT_e and its variation we decided to use the thermal Comptonization model $xillverCP$ (García et al. 2014). This model that takes into account the emission lines assuming it to be originating from disk reflection includes the Comptonization

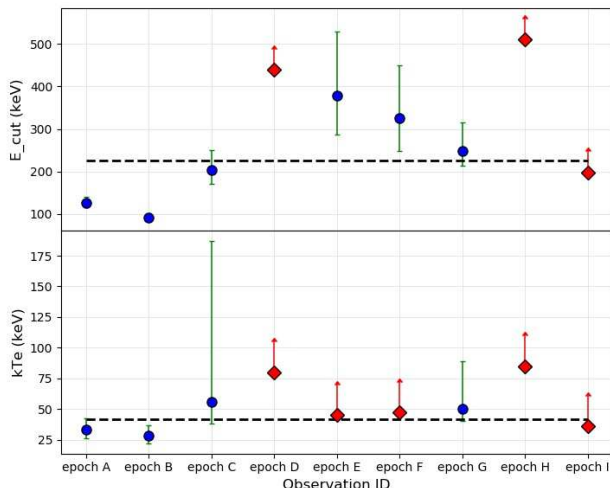


Fig. 6. Variation of E_{cut} and kT_e with the observation epochs as obtained from *xillver* and *xillverCP* model fit respectively to the spectra NGC 3227. The plotted errors were calculated using the $\chi^2 = 2.71$ criterion i.e. 90% confidence range. The black dashed lines in each panel are fits of constant (mean of E_{cut} and kT_e) to the data points. For the fitting, epochs in which we were unable to constrain E_{cut} and kT_e were dropped (indicated with red point).

model *nthcomp* (Zdziarski et al. 1996; Życki et al. 1999) plus the ionized reflection model *xillver* (García & Kallman 2010; García et al. 2013). The model fit to the spectra has the following form in XSPEC,

$$\text{const} * TBabs(\text{xillverCP}) \quad (6)$$

We used *xillverCP* to model the primary continuum and the reflection spectrum simultaneously. Also, to take care of the intrinsic absorption present in all epochs of NGC 5548, epoch G, H and I of NGC 3227 and epoch E of MR 2251–178 spectra the *zTBabs* component was added with the described model. The results of the model fits are given in Tables 2, 3 and 4.

4. Results and Discussion

Here, we aimed to find changes of kT_e in NGC 3227, NGC 5548 and MR 2251–178. We discuss below the results obtained on them.

4.1. NGC 3227

NuSTAR observed this source nine times between November 2016 and December 2019. Of these, results on seven epochs were reported by Kang et al. (2021), wherein they were able to constrain E_{cut} in three epochs using phenomenological fits and kT_e in two epochs using physical model fits. Here, we report results for two additional epochs and for all the nine epochs, we used both phenomenological and physical model fits to model the spectra.

Ratios of the model *const*TBabs(zpo + zgauss)*, *const*TBabs(pexrav + zgauss)* and *const*TBabs(xillverCP)* fits to the observed FPMA and FPMB spectra carried out on the OBSID 60202002002, the one with the longest exposure time are shown in Fig. 2. Weak FeK α line is present

in all the OBSIDs and therefore in the *const*TBabs(zpo)* and *const*TBabs(pexrav)* model fits we included a *zgauss* component to account for the line. All the above models could fit the spectra of all epochs of NGC 3227 reasonably well except for epochs G, H and I, where the χ^2/dof was greater than 1.2 and there is evidence for the presence of significant absorption at the low energy end (see Fig. 5). Addition of an extra absorption component *zTBabs* that takes into account the effects of host galaxy absorption to all the models improved the fit significantly (see left, middle and right panel of Fig. 8). The *const*TBabs(pexrav + zgauss)* model fit to the FPMA/FPMB spectra showed evidence for variation in E_{cut} . To analyze the variation of E_{cut} with time as well as to find the relation between E_{cut} and kT_e we used the E_{cut} values obtained from *xillver* model fits. The lowest value of E_{cut} of 92^{+10}_{-8} keV was obtained in epoch B and the highest value of E_{cut} was observed in epoch E (378^{+152}_{-91} keV) while intermediate values of E_{cut} were obtained during other epochs. These observed variation of E_{cut} indicates that the coronal temperature of NGC 3227 must be changing with time. This is also evident in Fig. 6 (upper panel) where the values of E_{cut} are plotted against epochs. To quantify the significance of the variation of E_{cut} we fitted a constant (mean of all the E_{cut} measurements) to the variation of E_{cut} with epoch and calculated the χ^2 and the null hypothesis probability (p) that E_{cut} does not change with time (shown as a dashed line in the top panel of Fig. 6). We found $\chi^2/\text{dof} \gg 10$, and a p value of 0.0 that the E_{cut} does not change with time. The values of E_{cut} obtained during the first two epochs (A and B) are similar to the value of $E_{\text{cut}} = 90 \pm 20$ keV reported by Markowitz et al. (2009). Vasudevan et al. (2013a) from an analysis of XMM and BAT spectra pointed E_{cut} to lie outside the BAT range at > 636 keV. Recently Kang et al. (2021) too reported E_{cut} values for epoch A, B and G, and lower limits for epochs C, D, E and F from *pexrav* model fits. The values of E_{cut} obtained here using *xillver* for epochs A, B and G are in agreement with that of Kang et al. (2021) from using *pexrav* model. Also, our model fits could constrain E_{cut} during epochs E and F using *xillver*.

Comptonization model fits using *xillverCP* provided values of kT_e which too was found to vary between epochs. We could constrain kT_e for epochs A, B, C and G, and obtain lower limits for epochs D, E, F, H and I. Kang et al. (2021) using the same model used here could constrain kT_e for only epochs A and B. Our results for epochs A and B are in agreement with that of Kang et al. (2021). The variation of kT_e is shown in the lower panel of Fig. 6. The trend seen in the variation of kT_e with epochs is similar to the variation of E_{cut} . From Comptonization model fits we found the lowest value of $kT_e = 28^{+9}_{-6}$ keV during epoch B while the highest value of $kT_e = 56^{+131}_{-18}$ keV was obtained for epoch E. We obtained lower limits of kT_e of 80, 45, 47, 85 and 36 keV during epochs D, E, F, H and I respectively. Spectral fits using *xillverCP* along with the data to model ratio for all the epochs are shown in Figures 7 and 8. The results of the model fits are given in Table 2. To quantify the significance of the variation of kT_e we fitted a constant (mean of all the kT_e measurements) to the variation of kT_e with epoch and calculated the χ^2 and the null hypothesis probability (p) that kT_e does not change with time (shown as a dashed line in Fig. 6). We found χ^2/dof of 12.86, and a p value of 0.005 that kT_e does not change with time. The contour plots between Γ against kT_e and R

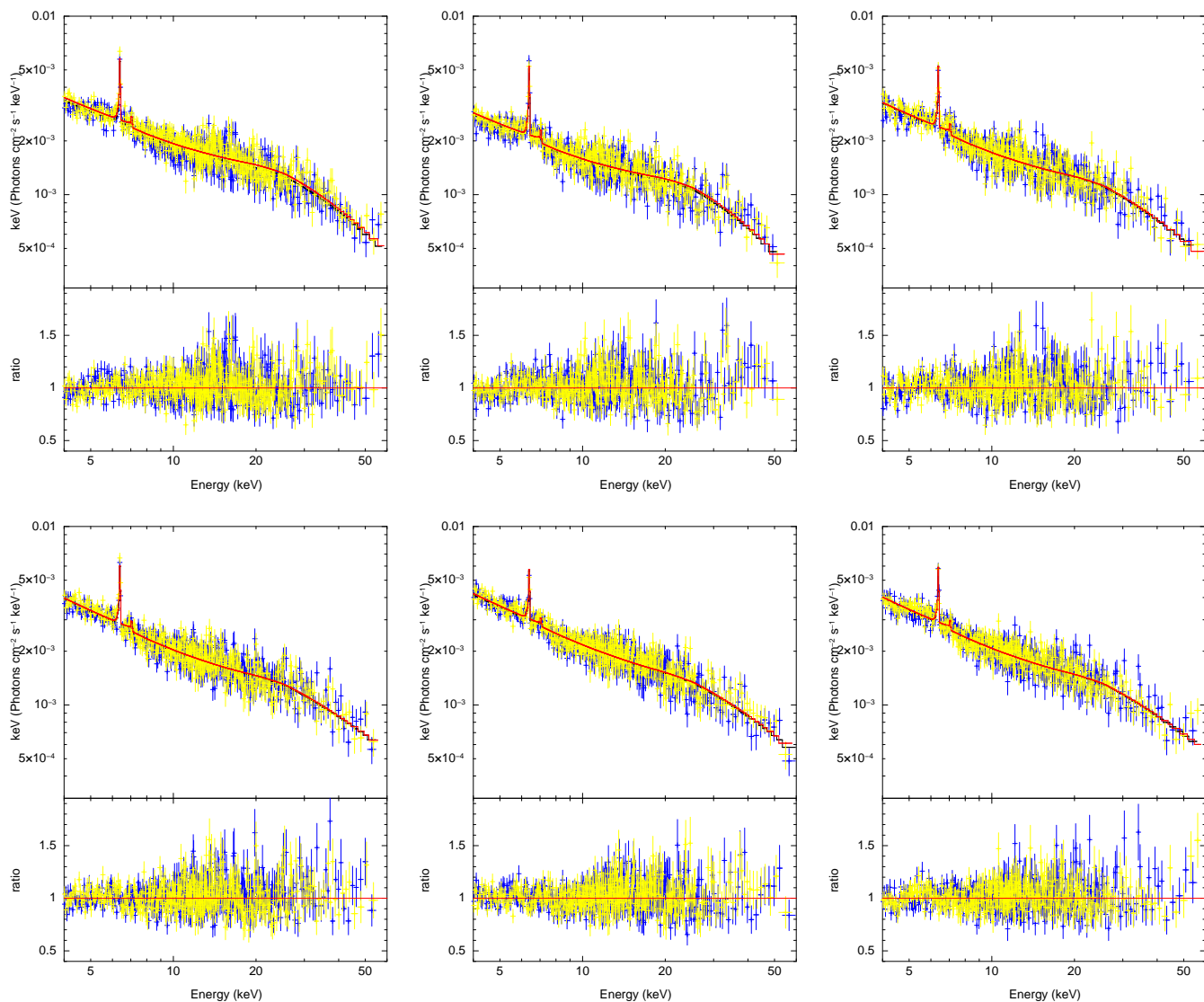


Fig. 7. The unfolded spectra along with $const^*TBabs(xillverCP)$ model fits and the data to model ratio for the epoch A (top left panel), epoch B (top middle panel), epoch C (top right panel), epoch D (bottom left panel), epoch E (bottom middle panel) and epoch F (bottom right panel) for the source NGC 3227. blue and yellow data points refer to FPMA and FPMB respectively.

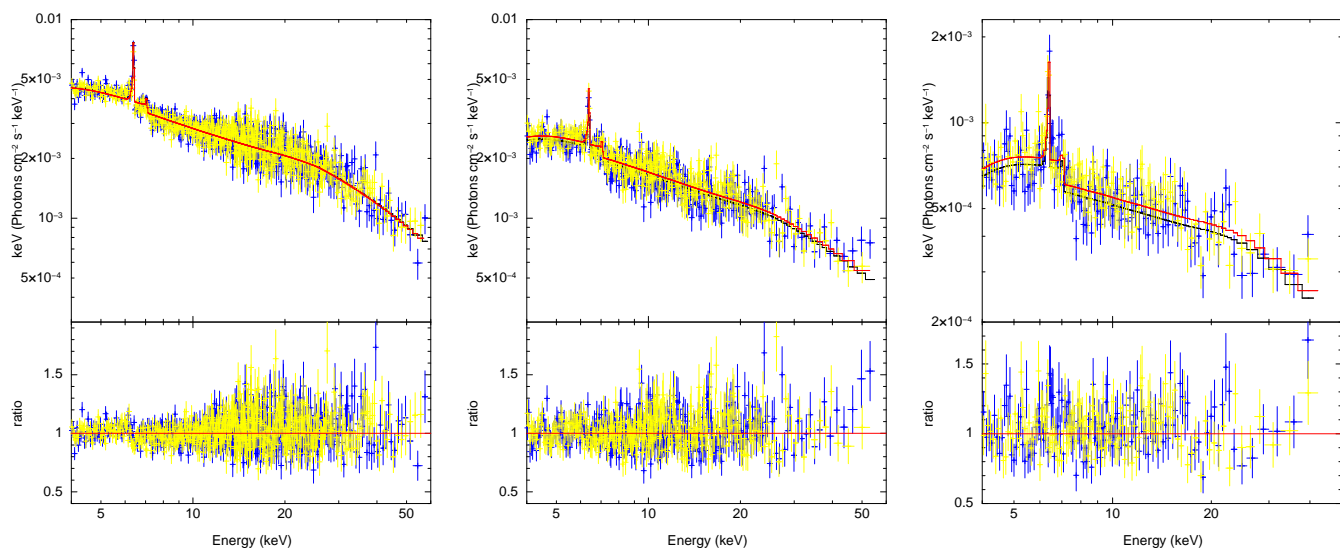


Fig. 8. The unfolded spectra and model fits along with the data to model ratio for $const^*TBabs(xillverCP)$ fits to the epoch G (left), epoch H (middle) and epoch I (right) of NGC 3227. For epoch G, epoch H and epoch I $zTBabs$ was added to the model. blue and yellow data points refer to FPMA and FPMB respectively.

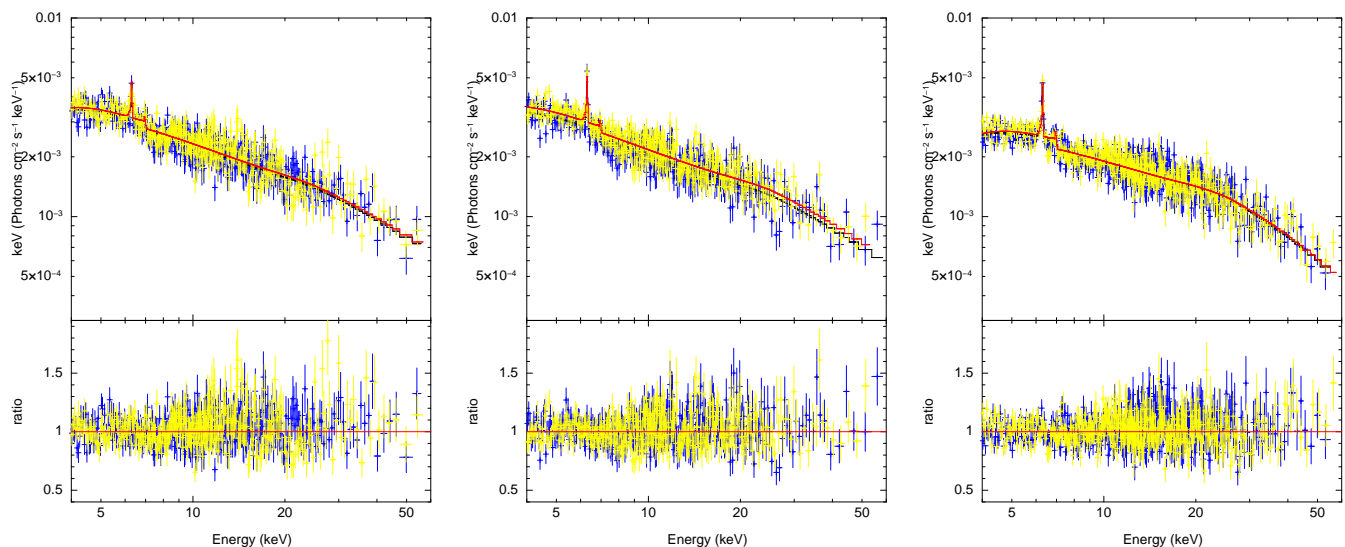


Fig. 9. The unfolded spectra with the $const*TBabs*zTBabs(xillverCP)$ model fits and the data to model ratio to the spectra of NGC 5548. Here epoch A is shown in the left panel, epoch B is shown in the middle panel and epoch C is shown in the right panel. Data from FPMA and FPMB are shown in blue and yellow respectively.

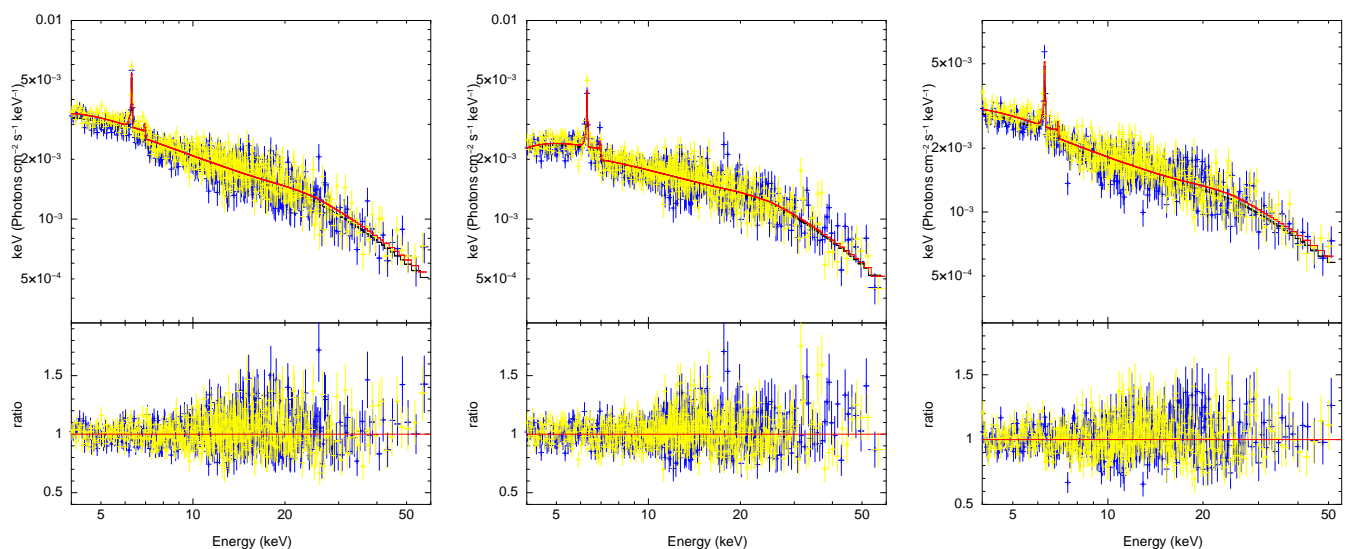


Fig. 10. The unfolded spectra with the $const*TBabs*zTBabs(xillverCP)$ model fits and the data to model ratio to the spectra of NGC 5548. Here the left, middle and right panels show the results for epochs D, E and F respectively. Data from FPMA and FPMB are shown in blue and yellow respectively.

against kT_e for NGC 3227 for all the epochs are shown in Fig. 14 and 15 (left panels). From the contour plots it is evident that the coronal temperature variation is prominent in NGC 3227. We therefore, conclude that we found variation in the temperature of the corona in NGC 3227. According to Petrucci et al. (2001) for an optically thick corona ($\tau > 1$) $E_{cut} = 3kT_e$. However, the relation between E_{cut} and kT_e can be complicated in the case of a non-static corona such as the one with outflows (Liu et al. 2014). Also, according to Middei et al. (2019), the relation of $E_{cut} = 2-3 kT_e$ is valid only for low values of τ and kT_e . For NGC 3227 using all the five epochs in which we could constrain both E_{cut} and kT_e we found $E_{cut} = 3.94 \pm 0.62 kT_e$ which is similar to that of Petrucci et al. (2001) and Middei et al. (2019)

4.2. MR 2251–178

This source has five epochs of observations that are public and having exposure > 20 ks. In this work we analyzed all of them. Simple power law fits to the FPMA spectra of all the epochs is shown in the right panel of Fig. 1. From this figure, noticeable change in the spectra could not be ascertained. The ratio of the model fits $const*TBabs(zpo)$, $const*TBabs(pexrav)$ and $const*TBabs(xillverCP)$ to the observed FPMA and FPMB spectra on OBSID 90601637002, the one with the longest exposure time are shown in Fig. 4. From two sets of observations from *Einstein* separated by about a year Halpern (1984) found evidence of variable X-ray absorption in MR 2251–178, with the column density changing from $< 5 \times 10^{21} \text{ cm}^{-2}$ to $2 \times 10^{22} \text{ cm}^{-2}$, suggested to be due to the presence of a warm absorber. *EXOSAT* and *Ginga* observations revealed strong correspondence between the ab-

Table 4. Results of the model fits to the spectra of NGC 5548. The models are Model I: $const*TBabs*zTBabs(zpo+zgauss)$, Model II: $const*TBabs*zTBabs(pearrav+zgauss)$, Model III: $const*TBabs*zTBabs(xillver)$ and Model IV: $const*TBabs*zTBabs(xillverCP)$. The width of the FeK α line was frozen to the value of 0.1 keV during the fitting. The fluxes are in units of 10^{-10} erg cm $^{-2}$ s $^{-1}$ in the 4–60 keV band except in epoch F where the flux was derived in 4–55 keV band. Columns and parameters have the same meaning as given in Table 2

Parameter	epoch A	epoch B	epoch C	epoch D	epoch E	epoch F
Model I : $const*TBabs*zTBabs(zpo+zgauss)$						
Γ	$1.62^{+0.03}_{-0.03}$	$1.60^{+0.03}_{-0.03}$	$1.59^{+0.02}_{-0.02}$	$1.64^{+0.02}_{-0.02}$	$1.57^{+0.03}_{-0.02}$	$1.57^{+0.03}_{-0.01}$
$N_H(zTBabs)$	$3.89^{+1.76}_{-1.73}$	< 3.21	$6.29^{+1.40}_{-1.32}$	$2.70^{+1.28}_{-1.27}$	$8.97^{+1.65}_{-1.63}$	< 1.28
E	$6.37^{+0.09}_{-0.09}$	$6.33^{+0.08}_{-0.08}$	$6.32^{+0.04}_{-0.04}$	$6.38^{+0.04}_{-0.04}$	$6.66^{+0.04}_{-0.04}$	$6.31^{+0.04}_{-0.04}$
EW	70^{+42}_{-23}	89^{+27}_{-31}	117^{+34}_{-34}	107^{+28}_{-29}	114^{+26}_{-44}	137^{+24}_{-45}
norm	100^{+10}_{-9}	86^{+11}_{-11}	79^{+8}_{-8}	93^{+7}_{-6}	77^{+6}_{-5}	67^{+5}_{-2}
χ^2/dof	684/643	612/634	880/811	890/813	840/810	692/692
$C_{FPMA/FPMB}$	$1.02^{+0.02}_{-0.02}$	$1.05^{+0.01}_{-0.01}$	$1.02^{+0.01}_{-0.01}$	$1.05^{+0.01}_{-0.01}$	$1.02^{+0.01}_{-0.01}$	$1.05^{+0.01}_{-0.01}$
Model II : $const*TBabs*zTBabs(pearrav+zgauss)$						
Γ	$1.75^{+0.02}_{-0.10}$	$1.81^{+0.02}_{-0.08}$	$1.62^{+0.10}_{-0.10}$	$1.79^{+0.09}_{-0.09}$	$1.61^{+0.10}_{-0.11}$	$1.81^{+0.08}_{-0.09}$
$N_H(zTBabs)$	$6.06^{+1.58}_{-2.46}$	$4.77^{+1.31}_{-2.05}$	$5.61^{+2.34}_{-2.36}$	$4.46^{+2.13}_{-2.16}$	$6.91^{+2.45}_{-2.47}$	$3.66^{+1.18}_{-2.10}$
E_{cut}	>345	>502	152^{+158}_{-54}	>170	160^{+178}_{-58}	>414
R	$0.19^{+0.14}_{-0.11}$	$0.35^{+0.16}_{-0.14}$	$0.28^{+0.11}_{-0.10}$	$0.37^{+0.12}_{-0.11}$	$0.33^{+0.12}_{-0.10}$	$0.42^{+0.14}_{-0.13}$
E	$6.37^{+0.10}_{-0.10}$	$6.32^{+0.09}_{-0.10}$	$6.32^{+0.04}_{-0.04}$	$6.38^{+0.05}_{-0.05}$	$6.35^{+0.04}_{-0.04}$	$6.31^{+0.05}_{-0.05}$
EW	55^{+38}_{-27}	64^{+31}_{-46}	114^{+24}_{-38}	89^{+25}_{-20}	113^{+29}_{-34}	104^{+44}_{-27}
norm	126^{+7}_{-23}	125^{+15}_{-19}	79^{+18}_{-15}	118^{+23}_{-20}	73^{+17}_{-14}	103^{+3}_{-17}
χ^2/dof	675/641	588/632	834/809	840/811	780/808	652/690
$C_{FPMA/FPMB}$	$1.02^{+0.02}_{-0.02}$	$1.05^{+0.01}_{-0.01}$	$1.02^{+0.01}_{-0.01}$	$1.05^{+0.01}_{-0.01}$	$1.02^{+0.01}_{-0.01}$	$1.05^{+0.01}_{-0.01}$
Model III : $const*TBabs*zTBabs(xillver)$						
Γ	$1.75^{+0.02}_{-0.02}$	$1.78^{+0.02}_{-0.04}$	$1.68^{+0.02}_{-0.01}$	$1.77^{+0.01}_{-0.01}$	$1.66^{+0.01}_{-0.02}$	$1.81^{+0.01}_{-0.01}$
$N_H(zTBabs)$	$6.47^{+0.98}_{-0.91}$	$4.83^{+0.95}_{-0.91}$	$7.13^{+0.73}_{-0.73}$	$4.52^{+0.69}_{-0.67}$	$8.16^{+0.76}_{-0.75}$	$4.25^{+0.83}_{-0.81}$
E_{cut}	>487	>480	129^{+15}_{-13}	179^{+40}_{-23}	133^{+15}_{-13}	>395
R	$0.25^{+0.08}_{-0.08}$	$0.36^{+0.10}_{-0.09}$	$0.49^{+0.09}_{-0.08}$	$0.49^{+0.08}_{-0.08}$	$0.51^{+0.09}_{-0.08}$	$0.54^{+0.11}_{-0.10}$
norm	$4.35^{+0.10}_{-0.06}$	$3.61^{+0.47}_{-0.14}$	$2.20^{+0.03}_{-0.03}$	$2.47^{+0.03}_{-0.03}$	$2.07^{+0.04}_{-0.04}$	$2.70^{+0.04}_{-0.04}$
χ^2/dof	677/643	595/634	851/811	849/813	792/810	666/692
$C_{FPMA/FPMB}$	$1.02^{+0.02}_{-0.02}$	$1.05^{+0.01}_{-0.01}$	$1.02^{+0.01}_{-0.01}$	$1.05^{+0.01}_{-0.01}$	$1.02^{+0.01}_{-0.01}$	$1.05^{+0.01}_{-0.01}$
Model IV : $const*TBabs*zTBabs(xillverCP)$						
Γ	$1.77^{+0.02}_{-0.02}$	$1.80^{+0.02}_{-0.03}$	$1.79^{+0.01}_{-0.01}$	$1.85^{+0.01}_{-0.01}$	$1.77^{+0.01}_{-0.01}$	$1.84^{+0.01}_{-0.02}$
$N_H(zTBabs)$	$6.47^{+0.99}_{-0.91}$	$4.63^{+0.94}_{-0.92}$	$8.72^{+0.73}_{-0.74}$	$5.66^{+0.69}_{-0.68}$	$9.79^{+0.76}_{-0.75}$	$4.30^{+0.87}_{-0.92}$
kT_e	>53	>54	39^{+14}_{-10}	65^{+14}_{-24}	38^{+12}_{-9}	>65
R	$0.25^{+0.08}_{-0.09}$	$0.35^{+0.11}_{-0.08}$	$0.43^{+0.08}_{-0.08}$	$0.46^{+0.09}_{-0.08}$	$0.45^{+0.08}_{-0.08}$	$0.55^{+0.11}_{-0.11}$
norm	$3.46^{+0.05}_{-0.05}$	$2.95^{+0.34}_{-0.04}$	$2.23^{+0.03}_{-0.03}$	$2.46^{+0.03}_{-0.04}$	$2.07^{+0.03}_{-0.03}$	$2.34^{+0.08}_{-0.03}$
χ^2/dof	677/643	595/634	855/811	852/813	795/810	667/692
$C_{FPMA/FPMB}$	$1.02^{+0.02}_{-0.02}$	$1.05^{+0.01}_{-0.01}$	$1.02^{+0.01}_{-0.01}$	$1.05^{+0.01}_{-0.01}$	$1.02^{+0.01}_{-0.01}$	$1.05^{+0.01}_{-0.01}$
Flux	$1.23^{+0.01}_{-0.01}$	$1.11^{+0.01}_{-0.01}$	$1.02^{+0.01}_{-0.01}$	$1.05^{+0.01}_{-0.01}$	$0.96^{+0.01}_{-0.01}$	$0.92^{+0.01}_{-0.01}$

sorbing column density and the flux of the source with the low energy absorption decreasing with the increasing flux of the source. These observations were explained by variable absorption in photo-ionized gas along the line of sight (Mineo & Stewart 1993; Pan et al. 1990). However, Walter & Courvoisier (1992) from an analysis of the *EXOSAT* data argued that the variability seen in the source can be explained without invoking the presence of a warm absorber. From the ratio of the observed data to the model fit we did not find any signature of absorption that could affect the source spectra in all observations but in epoch E and to take care of this we added the $zTBabs$ component to all the four models in epoch E (see Fig 11 and 12). Model fits to the four sets of observations that span about five years using $const*TBabs(zpo)$ do not reveal the presence of FeK α line in the spectra, the reflection bump was also found to be either negligible or weak (see top panel

of Fig. 4), more likely due to poor S/N. However, the ratio plot for the model $const*TBabs(zpo)$ to the epoch D spectra revealed the presence of the FeK α line at around 6.4 keV. We therefore added a $zgauss$ component with the model and found the energy of the line at $6.49^{+0.37}_{-0.27}$ keV with a fixed width of 0.1 keV, letting the parameter free did not significantly improve the fit. For this source previously the FeK α line was reported to be present in the *Ginga* observations with an equivalent width of 125^{+100}_{-105} eV (Mineo & Stewart 1993). Relatively strong FeK α was also reported to be present in the *BeppoSAX* observation (Orr et al. 2001) and a narrow FeK α line was present in the *Chandra* observations (Gibson et al. 2005). From *BeppoSAX* observations in the 0.1–200 keV band, Orr et al. (2001) found a E_{cut} value of around 100 keV which is similar to that obtained here. To find evidence for the change in kT_e if any, we carried out fitting of the observations with

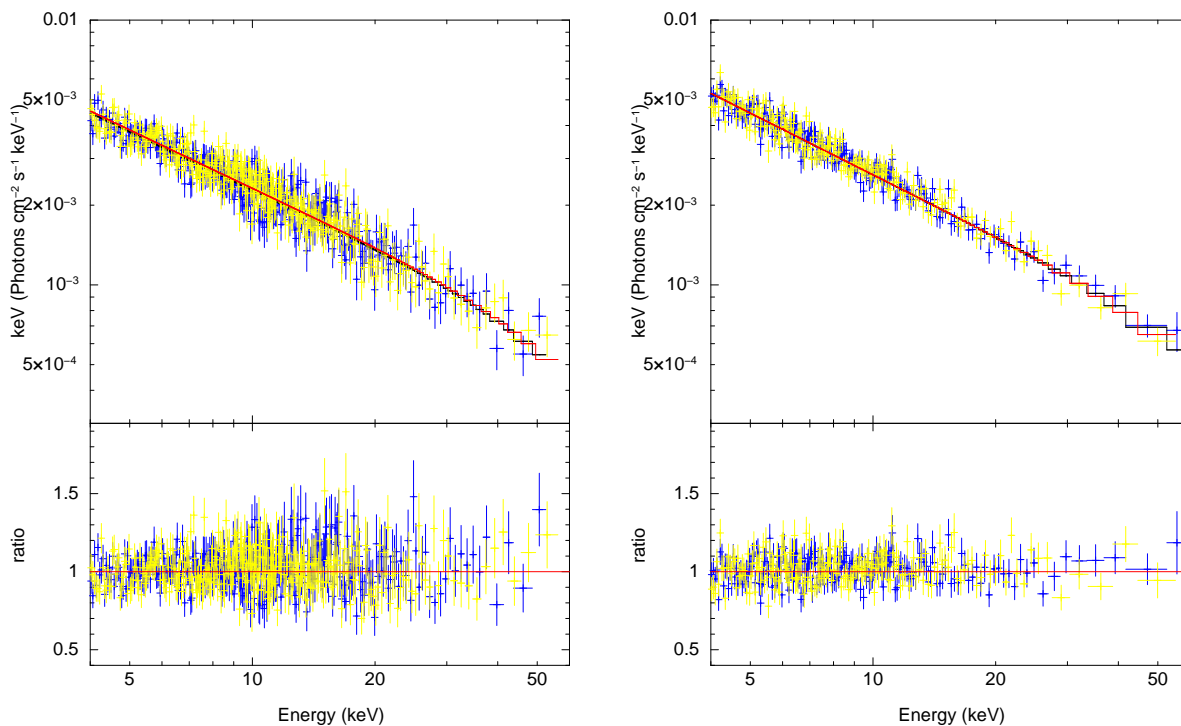


Fig. 11. The unfolded spectra along with the data to model ratio for $const*TBabs(xillverCp)$ fit to epoch A (left panel) and epoch B (right panel) observations of MR 2251–178. Here blue points are for FPMA and yellow points are for FPMB.

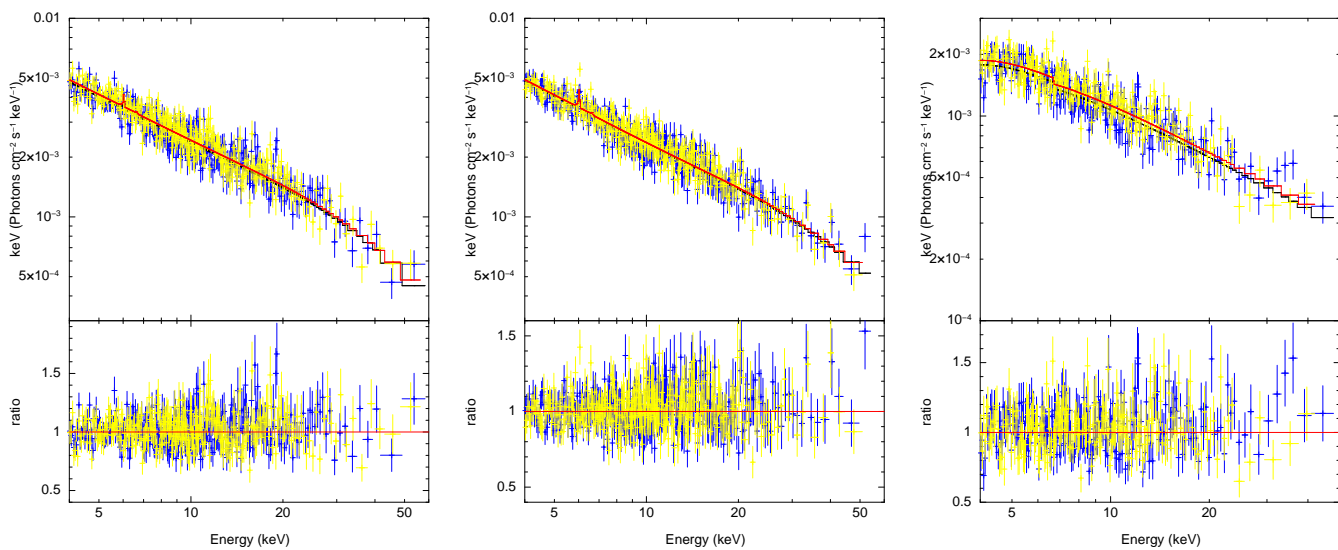


Fig. 12. The unfolded spectra along with the data to model ratio for $const*TBabs(xillverCp)$ fit to epoch C (left panel), epoch D (middle panel) and epoch E (right panel) observations of MR 2251–178. Here blue points are for FPMA and yellow points are for FPMB. In epoch E the $zTBabs$ component was added to the model.

the physical model, $const*TBabs(xillverCP)$. Examination of the results of the fit (Table 3) shows that the kT_e obtained during all the epochs agree within errors. Though we could not find any signature of kT_e variation with epochs from the $xillverCP$ fit, the E_{cut} values obtained from the $xillver$ model fit during epochs A, C and D agree within errors except that of epoch B. This could be due to the quality of the data in epoch B, as the values of E_{cut} and kT_e obtained during that epoch also have large error bars. To test for the kT_e variation if any, we plotted the 90 per cent contours between kT_e and Γ . The 90 percent contours of kT_e against Γ overlap (see Fig. 14) and we conclude that in MR 2251–178

we did not find any variation of kT_e with time. The 90 per cent contours of R against kT_e are also shown in the bottom panel of Fig. 15. Considering all the four epochs where E_{cut} and kT_e could be constrained we found $E_{cut} = 4.84 \pm 0.11$ kT_e . This is deviant from the generally adopted $E_{cut} = 2-3$ kT_e (Petrucci et al. 2001). It is likely the relation between E_{cut} and kT_e is complex and may depend on other physical properties of the sources. Homogeneous analysis of a large number of sources are needed to establish the relation between E_{cut} and kT_e as well as on its dependence on other physical properties. Spectral fits using $xillverCP$ along with the residuals for all the epochs are shown in Fig. 11 and 12.

Table 5. Results of the correlation analysis between different parameters for NGC 3227. Provided are the slope (m), intercept (c), Pearson’s correlation coefficient (r) and the probability (p) for null hypothesis (no correlation) from OLS fit and the least squares fit from simulated points. See text in Section 4.4.

Parameter	OLS				Simulated			
	m	c	r	p	m	c	r	p
Γ/Flux	-0.07 ± 0.03	1.90 ± 0.03	-0.63	0.07	-0.07 ± 0.03	1.91 ± 0.04	-0.64	0.06
kT_e/Flux	18 ± 28	22 ± 31	0.42	0.58	18 ± 150	13 ± 169	0.08	0.52
Γ/kT_e	0.001 ± 0.0006	1.75 ± 0.03	0.86	0.14	0.0005 ± 0.0002	1.78 ± 0.02	0.80	0.20
R/kT_e	-0.005 ± 0.005	1.03 ± 0.22	-0.57	0.43	-0.001 ± 0.002	0.90 ± 0.17	-0.36	0.60
R/Flux	-0.51 ± 0.13	1.31 ± 0.13	-0.84	0.01	-0.04 ± 0.15	0.78 ± 0.16	-0.09	0.68
τ/Flux	-0.29 ± 0.62	2.35 ± 0.65	-0.17	0.66	-0.98 ± 1.88	3.15 ± 2.12	-0.35	0.65
y/Flux	-0.15 ± 0.70	13.06 ± 0.79	-0.15	0.85	-0.53 ± 1.50	14.01 ± 1.71	-0.21	0.66
τ/kT_e	-0.043 ± 0.002	4.19 ± 0.09	-0.99	0.00	-0.02 ± 0.00	3.44 ± 0.28	-0.97	0.03

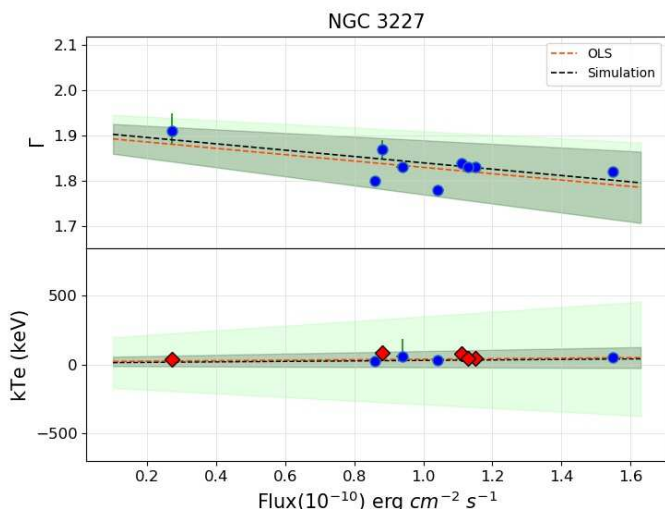


Fig. 13. Correlation of Γ and kT_e with the X-ray brightness of NGC 3227. The orange dashed line is the ordinary linear least squares (OLS) fit to the data points. The black dashed line is the linear line drawn using the median values of the simulated parameters. The grey shaded region indicates the upper and lower errors in the fit parameters for OLS and the green region indicates the errors in the fit parameter obtained from the simulation. In the least square analysis, epochs in which we were unable to constrain kT_e were dropped (indicated with red point).

4.3. NGC 5548

NGC 5548 was observed by *NuSTAR* six times between July 2013 to January 2021. Of these, Zhang et al. (2018) have reported results for five epochs. In this work we carried out both phenomenological and physical model fits for all the six epochs. We fit the spectra using *const*TBabs(zpo+zgauss)* and *const*TBabs(pearrav+zgauss)* to model the primary power law emission and the reflection component along with the FeK α line with the width of the line being frozen to the value of 0.1 keV. From the ratio of the observed data to the model fit using *TBabs* we found the presence of absorption component in the spectra. So unlike the other sources, for NGC 5548, we added an extra component *zTBabs* in each model to account for the absorption by the host galaxy. Moreover, as *xillver* self consistently models the reflected spectrum and its associated FeK α line, we also fit the spectra using *xillver* and E_{cut} values obtained using *xillver*

model were used to find variation in E_{cut} . The E_{cut} obtained from *xillver* model fits are > 487 keV, > 480 keV, 129^{+15}_{-13} keV, 179^{+40}_{-23} keV, 133^{+15}_{-13} and >394 keV for epochs A, B, C, D, E and F respectively. The residuals of the fit to the spectra for the epoch D that has the maximum exposure time, for various models are given in Fig. 3 and the results of the fit are given in Table 4. From *xillver* model fits, we could constrain E_{cut} only for epochs C, D and E, while Zhang et al. (2018) could constrain E_{cut} in the four epochs (A, C, D and E). For the epochs in common, though our values of E_{cut} are in agreement with Zhang et al. (2018) the results do not match for epoch E. Though Zhang et al. (2018) claims to have detected E_{cut} variation in NGC 5548, our analysis could not confirm changes in E_{cut} . This could be due to differences in the choice of binning and the energy ranges used in both the work. Ursini et al. (2015) via the joint fitting of *XMM-Newton*, *Chandra*, *NuSTAR*, and *INTEGRAL* data obtained lower limits for E_{cut} in all the epochs except for epoch D. Using the simultaneous *XMM-Newton* and *NuSTAR* data from 2013 campaign Cappi et al. (2016) also fitted the 4–79 keV epoch A/B, epoch D and epoch E spectra using cut-off power-law and *pearrmon*. Their values of E_{cut} are in agreement with the E_{cut} values obtained in this work.

Fitting the physical Comptonization model *xillverCP* to ascertain the change in coronal temperature, we got the highest kT_e value of 65^{+147}_{-24} keV during epoch D, for epochs A, B and F we obtained lower limits of 53, 54 and 71 keV, while for the remaining two epochs C and E, we obtained similar values of 39^{+14}_{-10} keV and 38^{+12}_{-9} keV respectively. The values of kT_e between epochs agree to each other within error bars. The model fits to the data along with the data to model ratio for all the epochs of observations are shown in Fig. 9 and 10. The E_{cut} values obtained here points to variability. However, the derived kT_e values are consistent with each other within error bars. The contour plots between kT_e against Γ as well as R against kT_e are shown in the right most panels of Fig. 14 and 15. From these plots, the change in kT_e is not evident. We thus conclude that we have not found evidence for variation in kT_e in NGC 5548. Considering all the epochs in which we could constrain both E_{cut} and kT_e , we found $E_{\text{cut}} = 3.19\pm 0.32 kT_e$ which is in agreement with the empirical relation of Petrucci et al. (2001).

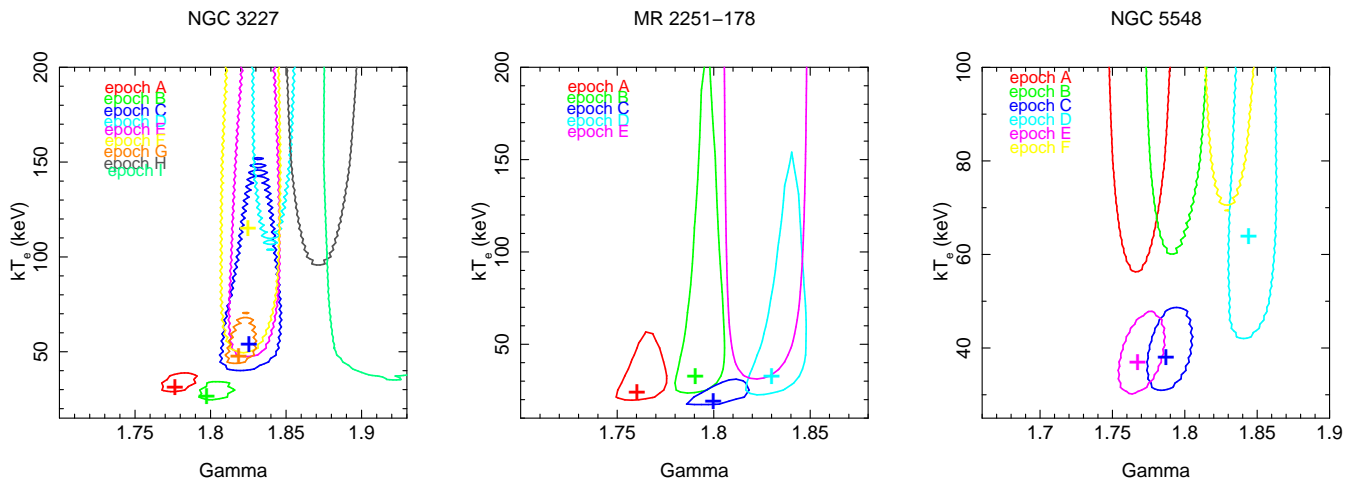


Fig. 14. The 90 per cent confidence level contours between kT_e and Γ for the *xillverCP* model fit to the FPMA/FPMB spectra of NGC 3227(left), MR 2251–178(middle) and NGC 5548(right). The colours indicate different OBSIDs. Here for MR 2251–178 the limits of kT_e do not have a correspondence with the values given in Table 3. This is because the contours were generated by freezing the R parameter so as to put all the five OBSIDs together.

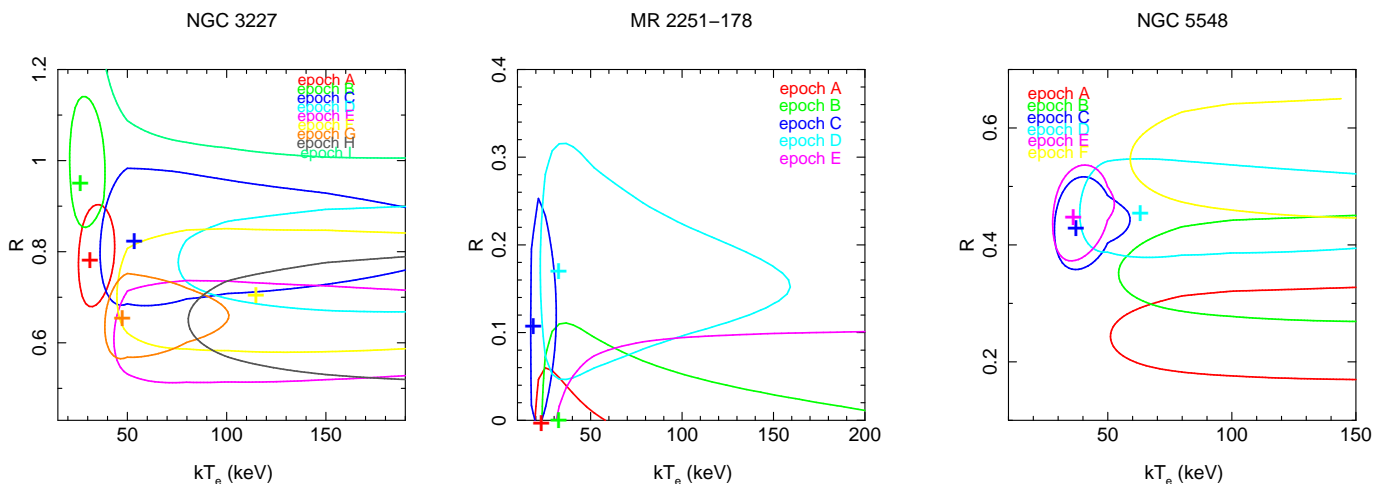


Fig. 15. The 90 per cent confidence level contours between R and kT_e for the *xillverCP* model fit to the FPMA/FPMB spectra of NGC 3227(left), MR 2251–178(middle) and NGC 5548(right).

4.4. Correlation between different parameters

We discuss below the correlation between various parameters. This is restricted to the source NGC 3227 as the temperature of its corona is found to vary in this work. Since the errors in the measured E_{cut} and kT_e values are not symmetric and there is no conventional way to take care of such errors during correlation study we adopted two procedures to find the correlation between various parameters.

In first case, we neglected the corresponding errors and considered only the best fit values of the parameters and performed the ordinary linear least square (OLS) fit between them. The Pearson’s correlation coefficient (r) and the null hypothesis probability (p) for no correlation were also estimated using the best fit values.

In the second case, to take into account the non-symmetric errors we simulated 10^5 points from each rectangular box around the best fit values (x, y) with x and y boundaries of ($x_{\text{low}}, x_{\text{high}}$) and ($y_{\text{low}}, y_{\text{high}}$) respectively. Here

x_{low} , y_{low} and x_{high} , y_{high} refer to the lower and upper errors in x and y values. Linear least squares fit was done for 10^5 times yielding distribution of the slope (m), the intercept (c), the Pearson’s rank correlation coefficient and the probability of no correlation. The median values of the distributions were taken to represent the best fit values of the correlation. All the values and the errors for the unweighted as well as for the simulated correlation are given in Table 5.

4.4.1. Γ v/s Flux

In Seyfert galaxies, the X-ray spectra are generally found to be softer with increasing X-ray flux (Markowitz et al. 2003). We show in Fig. 13, the correlation between Γ and the brightness of NGC 3227. For the source, each point in the Figure corresponds to Γ and flux obtained by *xillverCP* model fits to each epoch of spectra. Ordinary linear least

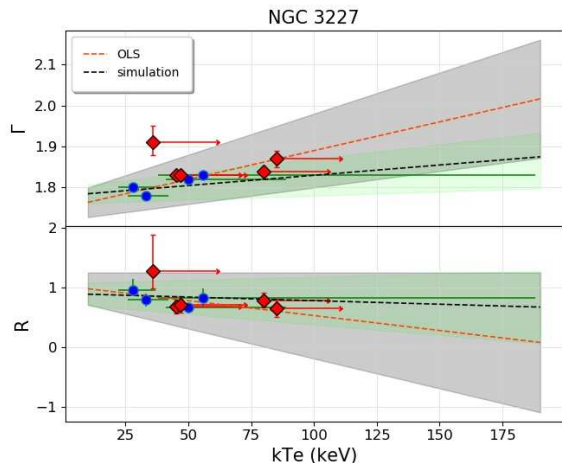


Fig. 16. Correlation between Γ and R with kT_e of NGC 3227. The dashed lines and shaded regions have the same meaning as in Fig. 13. Epochs in which kT_e could not be constrained (shown as red points) were not included in the linear least square analysis.

squares fit to the data are shown by orange dashed lines. The black dashed lines show the linear least square fit using the median values of the simulated points using the lower and upper errors in Γ and flux values. The grey and green shaded regions are the area bounded by the errors in the least square fit parameters. For NGC 3227, we found anti correlation between Γ and flux (see Fig. 13 and Table 5) between epochs of observations significant at the greater than 90 per cent level.

4.4.2. kT_e v/s Flux

Correlation between the changes in the temperature of the corona with other physical parameters of the sources such as its apparent brightness as well as its spectral shape can provide important constraints in enhancing our understanding of AGN corona. The correlation between kT_e and flux is shown in Fig. 13. Also, shown in the figure are the ordinary and simulated linear least squares fit to the data. No correlation is found between kT_e and flux in NGC 3227.

4.4.3. Γ v/s kT_e

In Fig. 16 the correlation between Γ and kT_e is shown. The orange and black dashed lines represent the ordinary and simulated least square fit to the data. The correlation between Γ and kT_e is found to be not significant.

4.4.4. R v/s kT_e

The correlation between the distant reflection fraction R and kT_e is presented in the bottom panel of Fig. 16. We did not find any correlation between these two parameters.

4.5. Nature of corona in AGN

The primary X-ray emission from thermal Comptonization depends on the optical depth τ and kT_e as (Zdziarski et al.

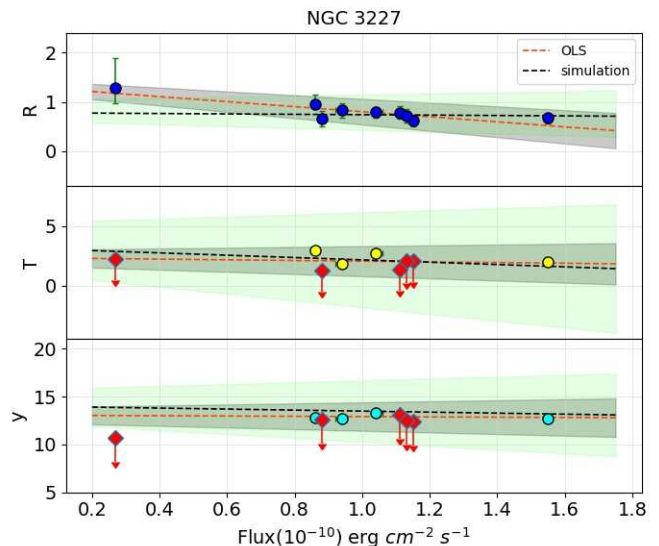


Fig. 17. Distant reflection fraction R , the optical depth τ and Compton- y parameter as a function of flux for the sources NGC 3227. The dashed lines and the shaded regions have the same meaning as in Fig. 13. Points shown as red in the Figure were not included in the linear least squares fit.

1996; Życki et al. 1999),

$$\tau = \sqrt{\frac{9}{4} + \frac{3}{\theta \left[\left(\Gamma + \frac{1}{2} \right)^2 - \frac{9}{4} \right]}} - \frac{3}{2} \quad (7)$$

where, $\theta = kT_e/m_e c^2$. We show in Fig. 18 the variation of the reflection fraction, the optical depth and the Compton “ y ” parameter with flux. The Compton y parameter is defined as (Petrucci et al. 2001),

$$y \simeq 4 \left(\frac{4kT_e}{mc^2} \right) \left[1 + \left(\frac{4kT_e}{mc^2} \right) \right] \tau (1 + \tau) \quad (8)$$

According to Stern et al. (1995), a Comptonized corona must have a constant y in equilibrium. We too found no correlation of y with the flux of the source. The parameter τ is found not to show any statistically significant variation with flux. R is found to be not correlated with flux (see Fig. 17).

Multiple epochs of observations on few AGN available today point to increased E_{cut} with the flux of the sources. For example, from analysis of *NuSTAR* and XMM-Newton observations of NGC 5548, Zhang et al. (2018) found E_{cut} to be positively correlated with the flux of the source. Similarly in Mrk 335 too, Keek & Ballantyne (2016) through joint fitting of *Suzaku* and *NuSTAR* found E_{cut} to be positively correlated with flux. Recently from flux resolved spectroscopy of Ark 564, Barua et al. (2020) found the temperature of the corona to decrease with increasing flux. Also, for the source ESO 103–035 Barua et al. (2021) found a positive correlation between kT_e and flux. Scenarios that could cause the change in the temperature of the corona or E_{cut} in AGN are (a) Compton cooling and (b) expanding corona. In the Compton cooling scenario, as the source brightens, there will be increased seed UV photons from the disk for Comptonization leading to a cooling of the corona. This leads to a

“cooler when brighter behaviour”. In the expanding corona scenario, the increase in kT_e during high flux states of the AGN could be due to changes in the geometry of the corona. This has been invoked to explain the E_{cut} changes in Mrk 335 (Keek & Ballantyne 2016) and NGC 5548 (Zhang et al. 2018). According to the expanding corona model, at low flux state, the corona is warm, optically thick, compact and close to the black hole. This causes more illumination of the disk leading to larger reflection fraction. As the source increases in brightness, the corona expands, the optical depth drops and the temperature rises. A reduced reflection fraction during this period argues that the corona expands vertically from the disk. In NGC 3227 too, the corona temperature is found to vary with time. We found a negative correlation between the optical depth τ and kT_e , with τ decreasing towards higher temperatures (see Fig. 18). We calculated τ using Equation 7 and according to Zdziarski et al. (1996) τ is geometry dependent and equals the radial optical depth in a uniform sphere. The negative correlation between τ and kT_e argues for a change in the geometry of the corona (Ballantyne et al. 2014). Tortosa et al. (2018) too from the analysis of a sample of AGN found a negative correlation between τ and kT_e . According to the authors this negative correlation could not be explained with a fixed disk-corona configuration in radiative balance. The possible explanation for this kind of behaviours could be (a) due to the change in the geometry and position of the corona and/or (b) variation in the fraction of the intrinsic disk emission to the total disk emission. We note that broad band spectral energy distribution fits to simultaneous UV to hard X-ray data alone will be able to provide strong constrain on τ . This in turn can put constraints on the role of accretion disk emission to kT_e changes. In NGC 3227 we found no statistically significant correlation between kT_e and flux, R and flux, Γ and flux as well as Γ and kT_e .

5. Summary

In this work, we carried out spectral analysis of the *NuSTAR* data for three Seyfert type AGN namely NGC 3227, NGC 5548 and MR 2251–178 including a few OBSIDs not analyzed yet in comparison to previous works. We summarize our results below

1. All the sources were found to show moderate variations in their average brightness during the epochs analyzed in this work.
2. In NGC 3227, we found unambiguous evidence for the change in the temperature of the corona. This change in kT_e is also reflected in the variation in E_{cut} . For NGC 5548 and MR 2251–178 we found no evidence for the variation in the temperature of the corona.

Our knowledge on the variation in the temperature of the corona is known only for less than half a dozen sources. Details on such coronal temperature variation in more AGN are needed to pin point the reasons for the temperature of the corona to vary and its effect on the other physical properties of the sources.

6. Acknowledgements

We thank the anonymous referee for her/his useful comments and suggestions which improved the quality and the

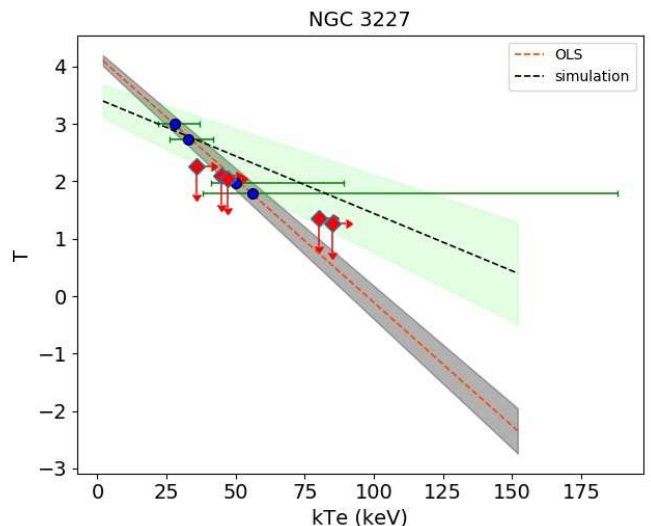


Fig. 18. Correlation between τ and kT_e of NGC 3227. The dashed lines and the shaded regions have the same meaning as in Fig. 13. Points shown as red in the Figure were not considered for the linear least squares fit.

clarity of the paper. We thank the *NuSTAR* Operations, Software and Calibration teams for support with the execution and analysis of these observations. This research has made use of the *NuSTAR* Data Analysis Software (NuSTARDAS) jointly developed by the ASI Science Data Center (ASDC, Italy) and the California Institute of Technology (USA). This research has made use of data and/or software provided by the High Energy Astrophysics Science Archive Research Center (HEASARC), which is a service of the Astrophysics Science Division at NASA/GSFC.

References

- Alonso-Herrero, A., García-Burillo, S., Pereira-Santaella, M., et al. 2019, *A&A*, 628, A65
- Arnaud, K. A. 1996, *Astronomical Society of the Pacific Conference Series*, Vol. 101, *XSPEC: The First Ten Years*, ed. G. H. Jacoby & J. Barnes, 17
- Ballantyne, D. R. 2020, *MNRAS*, 491, 3553
- Ballantyne, D. R., Bollenbacher, J. M., Brenneman, L. W., et al. 2014, *ApJ*, 794, 62
- Ballantyne, D. R. & Xiang, X. 2020, *MNRAS*, 496, 4255
- Baloković, M., Harrison, F. A., Madejski, G., et al. 2020, *ApJ*, 905, 41
- Barua, S., Jithesh, V., Misra, R., et al. 2020, *MNRAS*, 492, 3041
- Barua, S., Jithesh, V., Misra, R., et al. 2021, *ApJ*, 921, 46
- Bentz, M. C. & Katz, S. 2015, *PASP*, 127, 67
- Bergeron, J., Boksenberg, A., Dennefeld, M., & Tarengi, M. 1983, *MNRAS*, 202, 125
- Bhayani, S. & Nandra, K. 2011, *MNRAS*, 416, 629
- Bianchi, S., Guainazzi, M., Matt, G., Fonseca Bonilla, N., & Ponti, G. 2009, *A&A*, 495, 421
- Cappi, M., De Marco, B., Ponti, G., et al. 2016, *A&A*, 592, A27
- Chartas, G., Kochanek, C. S., Dai, X., Poindexter, S., & Garmire, G. 2009, *ApJ*, 693, 174
- Crummey, J., Fabian, A. C., Gallo, L., & Ross, R. R. 2006, *MNRAS*, 365, 1067
- Dadina, M. 2007, *A&A*, 461, 1209
- Della Ceca, R., Tagliaferri, G., Ghisellini, G., et al. 2010, in *AAS/High Energy Astrophysics Division*, Vol. 11, *AAS/High Energy Astrophysics Division #11*, 7.08
- Dewangan, G. C., Mathur, S., Griffiths, R. E., & Rao, A. R. 2008, *ApJ*, 689, 762
- Done, C., Davis, S. W., Jin, C., Blaes, O., & Ward, M. 2012, *MNRAS*, 420, 1848

- Fabian, A. C. 1999, *Proceedings of the National Academy of Science*, 96, 4749
- Fabian, A. C., Ballantyne, D. R., Merloni, A., et al. 2002, *MNRAS*, 331, L35
- Fabian, A. C., Lohfink, A., Belmont, R., Malzac, J., & Coppi, P. 2017, *MNRAS*, 467, 2566
- Fabian, A. C., Zoghbi, A., Ross, R. R., et al. 2009, *Nature*, 459, 540
- García, J., Dauser, T., Lohfink, A., et al. 2014, *ApJ*, 782, 76
- García, J., Dauser, T., Reynolds, C. S., et al. 2013, *ApJ*, 768, 146
- García, J. & Kallman, T. R. 2010, *ApJ*, 718, 695
- García, J. A., Kara, E., Walton, D., et al. 2019, *ApJ*, 871, 88
- George, I. M. & Fabian, A. C. 1991, *MNRAS*, 249, 352
- George, I. M., Mushotzky, R., Turner, T. J., et al. 1998, *ApJ*, 509, 146
- Gibson, R. R., Marshall, H. L., Canizares, C. R., & Lee, J. C. 2005, *ApJ*, 627, 83
- Gliozzi, M. & Williams, J. K. 2020, *MNRAS*, 491, 532
- Haardt, F. & Maraschi, L. 1991, *ApJ*, 380, L51
- Haardt, F., Maraschi, L., & Ghisellini, G. 1994, *ApJ*, 432, L95
- Halpern, J. P. 1984, *ApJ*, 281, 90
- Harrison, F. A., Craig, W. W., Christensen, F. E., et al. 2013, *ApJ*, 770, 103
- Jin, C., Ward, M., Done, C., & Gelbord, J. 2012, *MNRAS*, 420, 1825
- Johnson, W. N., McNaron-Brown, K., Kurfess, J. D., et al. 1997, *ApJ*, 482, 173
- Kaastra, J. S., Kriss, G. A., Cappi, M., et al. 2014, *Science*, 345, 64
- Kang, J.-L., Wang, J.-X., & Kang, W.-Y. 2021, *MNRAS*, 502, 80
- Keek, L. & Ballantyne, D. R. 2016, *MNRAS*, 456, 2722
- Komossa, S. & Fink, H. 1997, *A&A*, 327, 483
- Lanzuisi, G., Gilli, R., Cappi, M., et al. 2019, *ApJ*, 875, L20
- Liu, T., Wang, J.-X., Yang, H., Zhu, F.-F., & Zhou, Y.-Y. 2014, *ApJ*, 783, 106
- Lobban, A. P., Turner, T. J., Reeves, J. N., Braitto, V., & Miller, L. 2020, *MNRAS*, 494, 5056
- Lubiński, P., Beckmann, V., Gibaud, L., et al. 2016, *MNRAS*, 458, 2454
- Lubiński, P., Zdziarski, A. A., Walter, R., et al. 2010, *MNRAS*, 408, 1851
- Macchetto, F., Colina, L., Golombek, D., Perryman, M. A. C., & di Serego Alighieri, S. 1990, *ApJ*, 356, 389
- Magdziarz, P., Blaes, O. M., Zdziarski, A. A., Johnson, W. N., & Smith, D. A. 1998, *MNRAS*, 301, 179
- Malizia, A., Molina, M., Bassani, L., et al. 2014, *ApJ*, 782, L25
- Markowitz, A., Edelson, R., Vaughan, S., et al. 2003, *ApJ*, 593, 96
- Markowitz, A., Reeves, J. N., George, I. M., et al. 2009, *ApJ*, 691, 922
- Matt, G., Fabian, A. C., & Ross, R. R. 1993, *MNRAS*, 262, 179
- Matzou, G. A., Nardini, E., Parker, M. L., et al. 2020, *MNRAS*, 497, 2352
- McHardy, I. M., Gunn, K. F., Uttley, P., & Goad, M. R. 2005, *MNRAS*, 359, 1469
- Mehdipour, M., Kaastra, J. S., Kriss, G. A., et al. 2015, *A&A*, 575, A22
- Mehdipour, M., Kriss, G. A., Kaastra, J. S., et al. 2021, *A&A*, 652, A150
- Middei, R., Bianchi, S., Marinucci, A., et al. 2019, *A&A*, 630, A131
- Middei, R., Petrucci, P. O., Bianchi, S., et al. 2020, *A&A*, 640, A99
- Middleton, M. J., Parker, M. L., Reynolds, C. S., Fabian, A. C., & Lohfink, A. M. 2016, *MNRAS*, 457, 1568
- Mineo, T. & Stewart, G. C. 1993, *MNRAS*, 262, 817
- Mushotzky, R. F., Done, C., & Pounds, K. A. 1993, *ARA&A*, 31, 717
- Nandra, K., O'Neill, P. M., George, I. M., & Reeves, J. N. 2007, *MNRAS*, 382, 194
- Netzer, H., Turner, T. J., & George, I. M. 1994, *ApJ*, 435, 106
- Nicastro, F., Piro, L., De Rosa, A., et al. 2000, *ApJ*, 536, 718
- Orr, A., Barr, P., Guainazzi, M., Parmar, A. N., & Young, A. J. 2001, *A&A*, 376, 413
- Pan, H. C., Stewart, G. C., & Pounds, K. A. 1990, *MNRAS*, 242, 177
- Petrucci, P. O., Gronkiewicz, D., Rozanska, A., et al. 2020, *A&A*, 634, A85
- Petrucci, P. O., Haardt, F., Maraschi, L., et al. 2001, *ApJ*, 556, 716
- Petrucci, P. O., Haardt, F., Maraschi, L., et al. 2000, *ApJ*, 540, 131
- Petrucci, P. O., Paltani, S., Malzac, J., et al. 2013, *A&A*, 549, A73
- Petrucci, P. O., Ursini, F., De Rosa, A., et al. 2018, *A&A*, 611, A59
- Porquet, D., Reeves, J. N., Matt, G., et al. 2018, *A&A*, 609, A42
- Rani, P. & Stalin, C. S. 2018a, *ApJ*, 856, 120
- Rani, P. & Stalin, C. S. 2018b, *Journal of Astrophysics and Astronomy*, 39, 15
- Rani, P., Stalin, C. S., & Goswami, K. D. 2019, *MNRAS*, 484, 5113
- Rees, M. J. 1984, *ARA&A*, 22, 471
- Reeves, J. N., Braitto, V., Porquet, D., et al. 2021, *MNRAS*, 500, 1974
- Ricci, C., Trakhtenbrot, B., Koss, M. J., et al. 2017, *ApJS*, 233, 17
- Ricci, C., Walter, R., Courvoisier, T. J. L., & Paltani, S. 2011, *A&A*, 532, A102
- Ricker, G. R., Clarke, G. W., Doxsey, R. E., et al. 1978, *Nature*, 271, 35
- Risaliti, G., Elvis, M., Fabbiano, G., Baldi, A., & Zezas, A. 2005, *ApJ*, 623, L93
- Risaliti, G., Nardini, E., Salvati, M., et al. 2011, *MNRAS*, 410, 1027
- Ross, R. R. & Fabian, A. C. 1993, *MNRAS*, 261, 74
- Róžańska, A., Malzac, J., Belmont, R., Czerny, B., & Petrucci, P. O. 2015, *A&A*, 580, A77
- Schmitt, H. R., Kinney, A. L., Storchi-Bergmann, T., Antonucci, & Robert. 1997, *ApJ*, 477, 623
- Shakura, N. I. & Sunyaev, R. A. 1973, *A&A*, 500, 33
- Stern, B. E., Poutanen, J., Svensson, R., Sikora, M., & Begelman, M. C. 1995, *ApJ*, 449, L13
- Tazaki, F., Ueda, Y., Terashima, Y., & Mushotzky, R. F. 2011, *ApJ*, 738, 70
- Tortosa, A., Bianchi, S., Marinucci, A., Matt, G., & Petrucci, P. O. 2018, *A&A*, 614, A37
- Turner, T. J., Reeves, J. N., Braitto, V., et al. 2018, *MNRAS*, 481, 2470
- Ursini, F., Boissay, R., Petrucci, P. O., et al. 2015, *A&A*, 577, A38
- Ursini, F., Petrucci, P. O., Matt, G., et al. 2016, *MNRAS*, 463, 382
- Vasudevan, R. V., Brandt, W. N., Mushotzky, R. F., et al. 2013a, *ApJ*, 763, 111
- Vasudevan, R. V., Mushotzky, R. F., & Gandhi, P. 2013b, *ApJ*, 770, L37
- Verner, D. A., Ferland, G. J., Korista, K. T., & Yakovlev, D. G. 1996, *ApJ*, 465, 487
- Véron-Cetty, M. P. & Véron, P. 2010, *A&A*, 518, A10
- Walter, R. & Courvoisier, T. J. L. 1992, *A&A*, 266, 57
- Wang, J., Mao, Y. F., & Wei, J. Y. 2009, *AJ*, 137, 3388
- Willingale, R., Starling, R. L. C., Beardmore, A. P., Tanvir, N. R., & O'Brien, P. T. 2013, *MNRAS*, 431, 394
- Wilms, J., Allen, A., & McCray, R. 2000, *ApJ*, 542, 914
- Xu, Y., García, J. A., Walton, D. J., et al. 2021, *ApJ*, 913, 13
- Zdziarski, A. A., Johnson, W. N., & Magdziarz, P. 1996, *MNRAS*, 283, 193
- Zdziarski, A. A., Poutanen, J., & Johnson, W. N. 2000, *ApJ*, 542, 703
- Zhang, J.-X., Wang, J.-X., & Zhu, F.-F. 2018, *ApJ*, 863, 71
- Zoghbi, A., Fabian, A. C., Reynolds, C. S., & Cackett, E. M. 2012, *MNRAS*, 422, 129
- Zoghbi, A., Matt, G., Miller, J. M., et al. 2017, *ApJ*, 836, 2
- Zycki, P. T. & Czerny, B. 1994, *MNRAS*, 266, 653
- Zycki, P. T., Done, C., & Smith, D. A. 1999, *MNRAS*, 309, 561